Extrinsic Measurement of Carbon Black Aggregate Distribution within a Fluoroelastomer Matrix from Nanoindentation Experiments

Paul Baral, C. Fradet, Florian Lacroix, Éric Le Bourhis, Gaylord Guillonneau, Guillaume Kermouche, Jean-Michel Bergheau, Jean-Luc Loubet

To cite this version:

Paul Baral, C. Fradet, Florian Lacroix, Éric Le Bourhis, Gaylord Guillonneau, et al.. Extrinsic Measurement of Carbon Black Aggregate Distribution within a Fluoroelastomer Matrix from Nanoindentation Experiments. ACS Applied Materials & Interfaces, 2020, 12 (5), pp.6716-6726. 10.1021/acsami.9b20286 . emse-04511430

HAL Id: emse-04511430
https://hal-emse.ccsd.cnrs.fr/emse-04511430v1

Submitted on 19 Mar 2024

Extrinsic Measurement of Carbon Black Aggregates Distribution within a Fluoroelastomer Matrix from Nanoindentation Experiments

Journal:	*ACS Applied Materials & Interfaces*
Manuscript ID	am-2019-20286d.R1
Manuscript Type:	Article
Date Submitted by the Author:	n/a
Complete List of Authors:	Baral, Paul; Ecole Centrale de Lyon Fradet, Clémence; Université de Tours Lacroix, Florian; Université de Tours Le Bourhis, Eric; Institut P' Guillonneau, Gaylord; Ecole Centrale de Lyon Kermouche, Guillaume; Mines Saint-Étienne Bergheau, Jean-Michel; ENISE Loubet, Jean-Luc; Ecole Centrale de Lyon

Extrinsic Measurement of Carbon Black Aggregates Distribution within a Fluoroelastomer Matrix from Nanoindentation Experiments

P. Baral,*[†,‡] C. Fradet,[¶,§] F. Lacroix,[¶] E. Le Bourhis,[§] G. Guillonneau,[†] G. Kermouche,[‡] J.-M. Bergheau,[‖] and J.-L. Loubet[†]

[†] *Univ. Lyon, Ecole Centrale de Lyon, CNRS UMR 5513 LTDS, F-69134, Ecully, France*

[‡] *Mines Saint Etienne, Université de Lyon, CNRS UMR 5307 LGF, Centre SMS, Saint Etienne, F42023, France*

[¶] *Laboratoire de Mécanique Gabriel Lamé, Université de Tours, Université d'Orléans, INSA Centre Val de Loire, Polytech Tours, 7 Avenue Marcel Dassault BP40, Tours, 37004, France*

[§] *Département Physique et Mécanique des Matériaux, Institut Pprime, CNRS-Université de Poitiers, Boulevard Marie et Pierre Curie, Futuroscope, 86962, France*

[‖] *Univ. Lyon, Ecole Nationale d'Ingénieurs de Saint Etienne, CNRS UMR 5513 LTDS, F-42023, Saint Etienne, France*

E-mail: paul.baral@ec-lyon.fr

Abstract

A novel extrinsic measurement of the particle surface distribution in a carbon black filled elastomer via nanoindentation is developed. This method is based on the measurement of the contact stiffness obtained from the Continuous Stiffness Measurement

(CSM) mode. The proposed tip-particle model is held by two main hypotheses: the particles do not deform significantly during indentation so that only the elastomer matrix elastically deforms; particles are physically bounded with the surrounding matrix. Therefore, when the tip enters in contact with a particle, the latter becomes a hard extension of the tip, able to deform the elastomer matrix. Finally, the evolution of measured contact stiffness is directly related to the increase of contact area between the tip-particles set and the elastomer matrix. The proposed model is validated through a numerical and an experimental study. Moreover, an evaluation of the measurements bias allows to correct the particle surface distribution. A good agreement is found between the distribution measured from TEM observations and nanoindentation measurements.

Keywords

Nanoindentation, Particles distribution, Elastomer, Heterogeneities, Stiffness

1 Introduction

Characterization of particles, aggregates or agglomerates dispersion and size distribution in a polymer matrix is of primary interest for the reinforced polymer community. Indeed, these aspects influence directly the mechanical (conservative modulus, hardness, ...),[1–4] electrical (conductivity)[5] or physical (glass transition and melting temperatures)[6] properties.

In the case of fluoroelastomers (FKM), a reinforcement of the matrix by nanoparticles or carbon black enhances their thermal resistance. This improvement allows the use of FKM elastomers in petrochemical industry, automotive, aeronautics and aerospace as seals, gaskets or O-rings used in extreme temperatures.[7–9]

Effects of the particles, aggregates or agglomerates can be characterized at different scales, from discrete to homogenized analysis. Therefore, several methods can be used to characterize, with high resolution, dispersion and size distribution of hard particles in a soft media:[10]

Transmission Electron Microscopy (TEM) is clearly the most accurate characterization method[11] with a resolution down to 0.05 nm. However, it requires the preparation of thin foils which is a difficult and expensive task with such soft media: Its use is therefore strongly limited. Small Angle X-Ray Scattering (SAXS) allows for the measurement of nanoparticles size over several nanometers length scale in an easier way[12–14] but it remains a global measurement technique and requires some mathematical inversion models and hypotheses on nanoparticle shape to estimate the nanoparticle size distribution. Also, Dynamic Light Scattering (DLS) allows to measure particles sizes ranging from 2 nm to 2 μm[15] with applications to translucent materials. Regarding mechanical measurement, Atomic Force Microscopy (AFM)[16] can evaluate local stiffness gradient with a spatial resolution down to 15 nm. Dispersion of particles can also be assessed by conductive probe AFM in contact mode[5] at the nanometric scale.

Nanoindentation results, for this kind of materials, are mainly interpreted as for homogenized solids with an intrinsic Indentation Size Effect (ISE)[2] related to the presence of hard bodies in the soft matrix for 100 nm to some microns. Yet, no attempt has been done to link the change in mechanical properties with the size and distribution of the concerned hard bodies. It is proposed here, with a simple model named "tip-particle", to bridge the gap between a fully discrete and a homogenized analysis by considering the participation of each particle (or aggregate and agglomerate) to the change in measured mechanical properties – i.e. contact stiffness.

The proposed tip-particle model is held by two main hypotheses: the particles do not deform significantly during indentation so that only the elastomer matrix elastically deforms and the particles are physically bounded with the surrounding matrix. Therefore, when the tip enters in contact with a particle, the latter becomes a hard extension of the tip, able to deform the elastomer matrix. Finally, the evolution of measured contact stiffness is directly related to the increase of contact area between the tip-particles set and the elastomer matrix.

First, experimental evidences of a carbon black-filled fluoroelastomer heterogeneity are detailed based on TEM observations and nanoindentation experiments. Then, a tip-particle model is proposed in order to better understand the contribution of the carbon black aggregates to the contact stiffness evolution during nanoindentation. This model is used to deduce from nanoindentation experiments, the distribution of particles' projected area in the carbon black-filled fluoroelastomer. Finally, the model is challenged and discussed with numerical simulation based on TEM observations and nanoindentation experiments.

2 Experimental section

2.1 Material

The studied material is a fluoroelastomer vulcanized with peroxide. Figure 1 shows a TEM image of FKM elastomer composed of a rubber matrix (light gray), small and well-dispersed carbon black agglomerates with diameter between 300 and 800 nm (black) and silicon agglomerates with typical size of several tens of nanometers (intermediate gray). White spots are voids in the sample which correspond to carbon black aggregates removed during the TEM specimen preparation. The composite material's glassy transition temperature, measured by Differential Scanning Calorimetry (DSC), is -17 °C. The conservative modulus, measured by Dynamic Mechanical Analysis (DMA) at 1 Hz and 0.01 % strain, is 15 MPa. For comparison, the Young modulus of carbon black nanoparticles have been measured around 9 GPa by nano-compression.[17]

The molded surface presents relatively large roughness of about Ra = 0.5 μm. Polishing methods being not appropriate due to degradation of the elastomer – even at low temperature –, we have developed a cross section cutting method allowing surface roughness of about Ra = 0.1 μm.

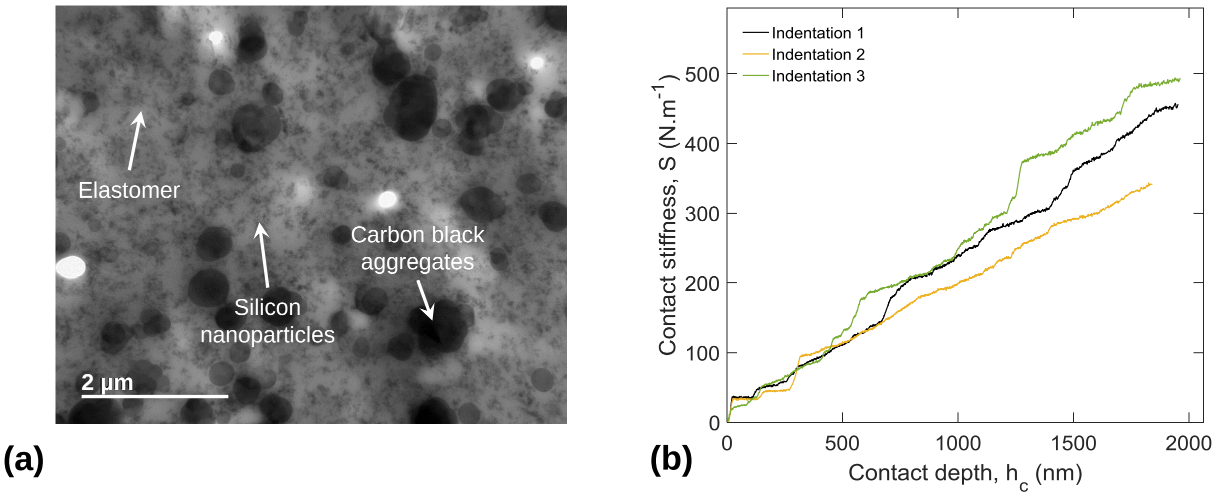

Figure 1: Experimental observations of heterogeneities in the elastomer: (a) Transmission Electron Microscopy observation of a 100 nm thick slice of elastomer and (b) evolution of contact stiffness during indentation as a function of contact depth.

2.2 Nanoindentation experiments

Nanoindentation experiments were performed with a Nanoindenter SA2® (Keysight Technologies, Santa Rosa, California) with a Dynamic Contact Module (DCM®) head that allows for very accurate measurements at low load and displacement. The indentation set-up is load-controlled with a maximum force of 10 mN and a resolution of 1 nN. Displacement is measured with a resolution of 0.2 pm.

Constant strain rate loadings have been performed on the carbon black-filled fluoroelastomer with a typical strain rate of $\dot{h}/h = 0.02$ s^{-1} and a maximum penetration depth of 1500 nm. The Berkovich diamond tip, used for this study, have a height defect of 6 nm, as determined in a previous study.[18] Constant strain rate experiments were reproduced ten times at different locations to exploit statistically the data. The Continuous Stiffness Measurement (CSM) module was used with an amplitude of 4 nm at 75 Hz to measure the stiffness as a function of time.

It has been assessed by several authors that contact area is proportional to the contact stiffness as long as the materials' modulus is not indentation depth-dependent. Hence, the following relation is used[19,20] :

$$S(\omega) = 2E_c'^*(\omega)\sqrt{\frac{A_c}{\pi}} \tag{1}$$

Where $S(\omega)$ and $E_c'^*(\omega)$ are the contact stiffness and the reduced contact modulus measured at a given frequency ω, and A_c is the contact area.

The evolution of contact stiffness with contact depth is represented in figure 1b. Theoretically, for a homogeneous material, the contact stiffness is directly proportional to the contact depth. However, when indenting a heterogeneous material, this relation is no longer valid and abnormal contact stiffness evolutions are measured (see figure 1b).

2.3 Tip-particle model

The tip-particle model is based on a simple hypothesis which states that all the deformation in the material is supported by the elastomer matrix. Hence, carbon black aggregates, which are two orders of magnitude stiffer and harder than the elastomer matrix, as described in section 2.1, do not significantly deform during indentation. Also, the mean pressure under the tip $p_m = F/A_c$, with F the load on sample and A_c the contact area does not exceed 100 MPa at shallow depth and goes down to around 0.8 MPa above 150 nm depth. This is significantly lower than the hardness of the carbon black aggregates and makes us confident that the latter should not be crushed or broken under the tip. As a consequence, when the diamond tip enters in contact with an aggregate, the latter becomes a hard extension of the tip capable to deform the elastomer matrix underneath. Furthermore, when an aggregate enters in contact with the tip, the contact area extension induces a sudden increase in contact stiffness. These events have been reported experimentally and are coherent with the present model.

The hypotheses of the model are listed below:

- All the deformation in the material is supported by the elastomer matrix.
- Particles do not significantly deform during indentation.
- Particles are physically bounded to the surrounding matrix.
- Particles are not in contact with each other.
- The adhesion between the tip, the particles and the matrix is negligible.
- An abnormal increase of the stiffness is attributed to a single particle entering in contact with the tip.

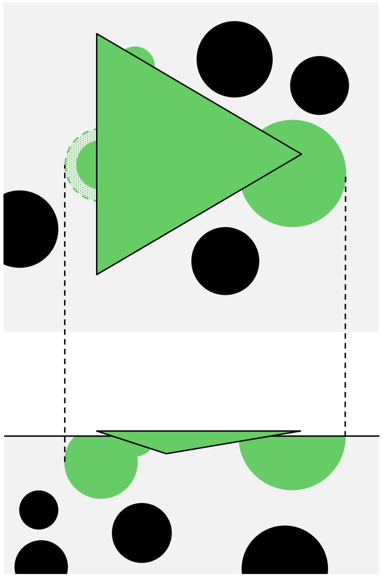

Figure 2: Example of the tip-particle model, with the black particles corresponding to carbon black aggregates and the gray part corresponding to the elastomer matrix. The green parts represent the area of the Berkovich tip and the particles in contact with the tip.

Figure 2 displays the tip-particle model basic principle, with the Berkovich tip in contact with the three particles highlighted in green.

2.4 Distribution of particles' projected area

The particle projected area distribution is extracted from the tip-particle model considering each stiffness jump as the combined participations of the homogeneous increase of contact area and the apparition of a particle in the contact. Hence, the total increment area ΔA_c – i.e. increment area from the indenter with the particles in contact – can be calculated from equation 1 as a function of the jump stiffness amplitude ΔS and the contact stiffness S just before the jump.

$$\Delta A_c = \frac{\pi}{4E_c'^{*2}}\left(2S\Delta S + \Delta S^2\right) \tag{2}$$

The projected area of the detected particle is written as:

$$A_{part} = \Delta A_c - \xi \Delta A_{c,\ hom} \tag{3}$$

$$\Delta A_{c,\ hom} = \frac{\pi}{4E_c'^{*2}}(S_{he}^2 - S_{hb}^2) \tag{4}$$

Where A_{part} is the particle size and $\Delta A_{c,\ hom}$ is the homogeneous increase of the contact considering only fluoroelastomer matrix. Moreover, S_{hb} and S_{he} are the stiffnesses in the case of a homogeneous material at the beginning and at the end of the jump, respectively. These stiffnesses are calculated with a linear relationship between S and h_c such as $S_h = \frac{2E_c'^{*}}{\tan(\beta)}h_c$, with h_c the contact depth, calculated from the Oliver and Pharr model,[19,21] and $\beta = 19.68°$ the inclined face angle of the Berkovich equivalent conical tip. In equation 3, the portion of indenter area removed from the total increment area is noted ξ. The meaning of ξ is illustrated on figure 3.a where, after an increment, the indenter touches a new particle (in light green). This new particle implies an increase in the stiffness measurement characterized by a segment in figure 3.b. ξ modifies the portion of the jump attributable to the new particle such as, for $\xi = 1$, 100 % of the new indenter perimeter is removed (see figure 3.c). This leads to a correct estimation of the particle area if no other particles are already in contact, but it leads to underestimation of its size otherwise. For $\xi = 0$, all the area responsible for the stiffness jump amplitude is associated to the particle (see figure 3.d). Here again, it is not right since a part of the stiffness jump amplitude is due to the increase of the indent size. Hence, the portion of stiffness jump attributable to one new particle is dependent on the number of particles already in contact at the periphery of the indenter. An estimation of ξ will be performed based on numerical simulation in the results section.

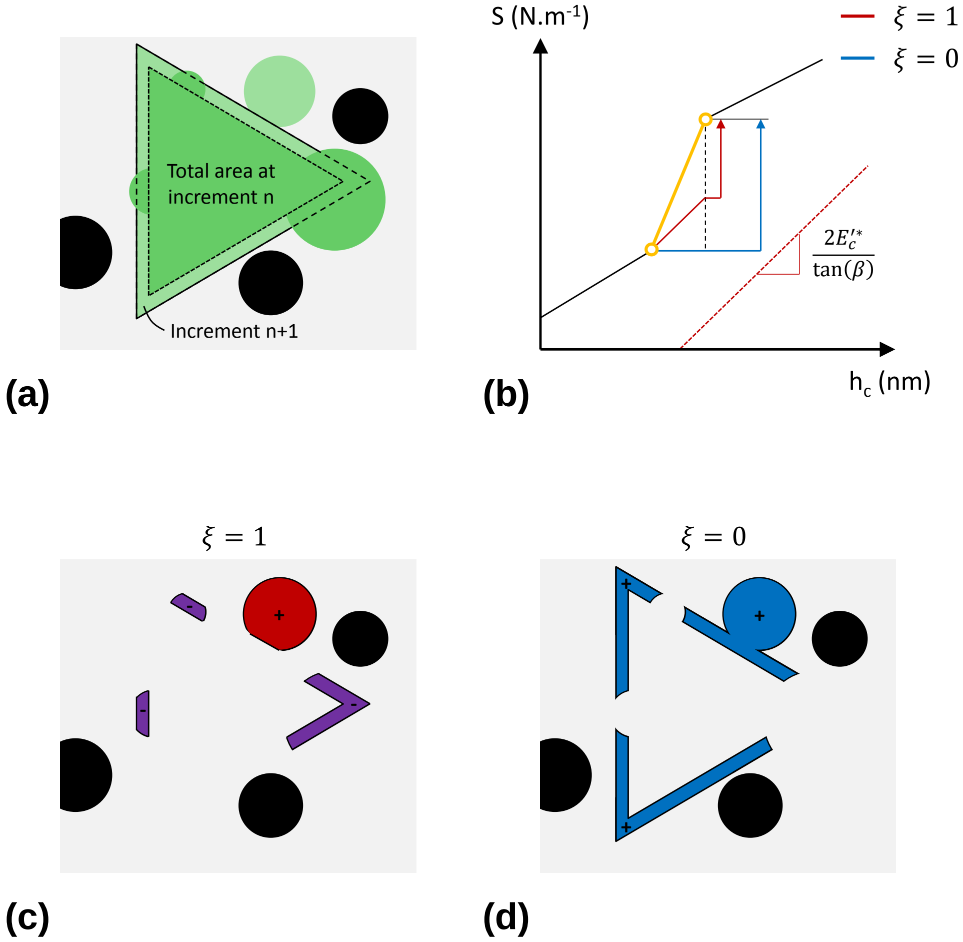

Figure 3: Schematic representation of an indent entering in contact with particles (a) and the different ways of considering the particle area: (c) residual area of the particle considering $\xi = 1$; (d) residual area of the particle considering $\xi = 0$ and (b) impact on the stiffness jump portion attributable to the particle.

2.5 Detection limitations due to the loading

If we consider that a stiffness jump is attributed to a single particle – i.e. without considering the homogeneous increase of the contact size during the jump, $\xi = 0$ – the range of detectable particle size can be derived from the expression 2. With a minimum stiffness amplitude detection ΔS_{min} in the equation 2, one can describe the minimum detectable area $A_{part} = \Delta A_c$ as a function of contact stiffness S – i.e. indentation depth. The following developments are written as a function of the total increment area ΔA_c for sake of uniformity with equation 2.

Then, considering the maximum stiffness attained during the experiment S_{max}, the detection limits for a given particle size are known. In other words, the minimum particle area detectable is a function of the contact area between the tip and the matrix – i.e. larger is the tip-elastomer contact size, higher is the minimum detectable particle area.

Figure 4 displays a diagram representing the detection space as a function of the particle size ΔA_c. This space is delimited by equation 5 for $\Delta A_c \in [\Delta A_{c,\ min}, \Delta A_{c,\ lim}]$ and by S_{max} for $\Delta A_c \in [\Delta A_{c,\ lim}, +\infty)$.

$$S(\Delta A_c) = \frac{2E_c'^{*2}}{\pi \Delta S_{min}} \Delta A_c - \frac{\Delta S_{min}}{2} \tag{5}$$

The different detection zones are the following:

- The first zone is delimited by $\Delta A_c \in [0, \Delta A_{c,\ min}[$ and corresponds to particle areas which cannot be detected due to the lower stiffness detection S_{min} ;
- The second zone is delimited by $\Delta A_c \in [\Delta A_{c,\ min}, \Delta A_{c,\ lim}[$ where the particles can be partially detected during the whole loading ;
- Finally, the third zone, delimited by $\Delta A_c \in [\Delta A_{c,\ lim}, +\infty)$, where the particles are fully detected. Hence, for particles areas greater than $\Delta A_{c,\ lim}$, no underestimation of their occurrences is due to the loading procedure.

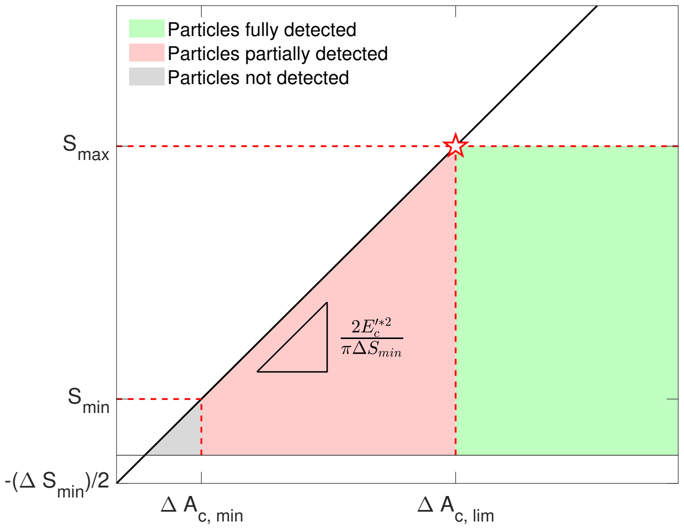

Figure 4: Detection space as a function of the particle size considered and of the stiffness parameters ΔS_{min} and S_{max}.

Therefore, the smallest particle detectable during a whole loading $\Delta A_{c,\ lim}$ is expressed from equation 2 such as:

$$\Delta A_{c,\ lim} = \frac{\pi}{2E_c'^{*2}} \left[S_{max} \Delta S_{min} + \frac{\Delta S_{min}^2}{2} \right] \tag{6}$$

In the case where the particles size are included between $\Delta A_{c,\ min}$ and $\Delta A_{c,\ lim}$, the same equation can be written by replacing S_{max} by S, with $S < S_{max}$. This relates the maximum stiffness S at which the considered particle area ΔA_c is detected. By extension, the maximum tip-elastomer contact area $A_c(S)$ is related to the considered particle area ΔA_c.

This means that for each particle area $\Delta A_c < \Delta A_{c,\ lim}$ the associated maximum tip-elastomer contact area $A_c(S)$ is lower than the contact at the end of loading $A_c(S_{max})$. Therefore, the concerned particle densities are underestimated because they are calculated based on a lower probed area.

Considering this, a correction can be applied to the measured particle densities with the hypothesis of a homogeneous distribution of the particles within the total probed area.

The measurement bias α is expressed as the ratio of the maximum tip-elastomer area $A_c(S)$ enabling the detection of a given particle area $\Delta A_c < \Delta A_{c,\ lim}$ over the final contact area $A_c(S_{max})$. Therefore, the measurement bias α is proportional to the square of the stiffness S, as written in equation 7. If $\alpha = 1$, there is no bias and if $\alpha < 1$ there is one.

$$\alpha = \frac{A_c(S)}{A_c(S_{max})} = \frac{S^2}{S_{max}^2} \tag{7}$$

Developing equation 7 with equation 5 as a function of particle area ΔA_c leads to a polynomial of the second order:

$$\alpha = \left[\left(\frac{2E_c'^{*2}}{\pi \Delta S_{min}} \right)^2 \Delta A_c^2 - \frac{2E_c'^{*2}}{\pi} \Delta A_c + \frac{\Delta S_{min}^2}{4} \right] \frac{1}{S_{max}^2} \tag{8}$$

Equation 8 expresses the measurement bias for each particle area lower than $\Delta A_{c,\ lim}$ as a function of S_{max} and ΔS_{min}. To correct a distribution of particle densities, represented as a histogram, an average of equation 8 must be done for each interval of particle size – i.e. $\Delta A_c \in [\Delta A_c(i), \Delta A_c(i+1)]$. This equivalent measurement bias is written α_{equ}.

Equation 8 is valid for $S(\Delta A_c) < S_{max}$. When $S(\Delta A_c) \geq S_{max}$, $\alpha = \alpha_{equ} = 1$. Figure 5 displays α from equations 8 and α_{equ} as a function of ΔA_c.

From these developments, the correction applied to the number of detected particles as a function of their sizes $N_{exp}(\Delta A_c)$ is expressed as follow:

$$N_{cor}(\Delta A_c) = \frac{N_{exp}(\Delta A_c)}{\alpha_{equ}} \tag{9}$$

With N_{cor} the number of particles corrected and N_{exp} the number of particles detected experimentally. This model prediction will be assessed in the following by means of numerical and experimental results.

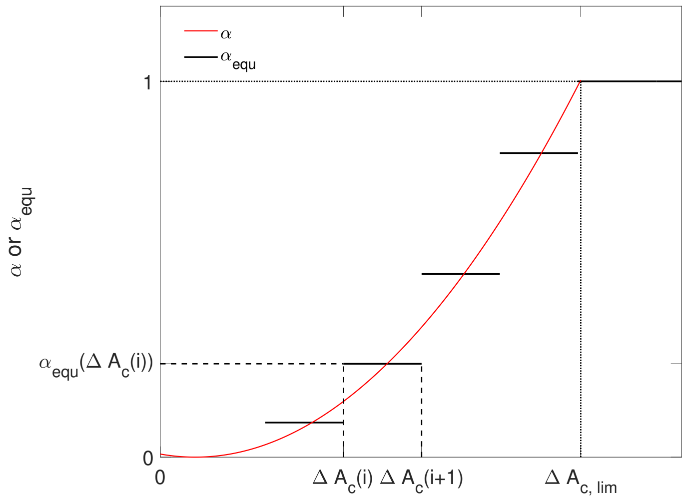

Figure 5: Measurement bias α and α_{equ}, expressed by equation 8 and from its interval average, respectively, as a function of particle area ΔA_c.

3 Results and discussion

3.1 Experimental stiffness measurements

As it has been described in previous section, stiffness measurements have been performed with the continuous stiffness measurement module available on the DCM® nanoindenter head. Contact stiffness is measured by oscillating the tip at targeted amplitude and frequency – i.e. 4 nm and 75 Hz. The method allows for very sensitive measurements of the contact stiffness as can be seen on figure 1b, even though some measurement noise exists.

Figure 6 displays the variation of stiffness around the general trend n_{stiff} calculated by a moving average on 18 points. The standard deviation of the stiffness noise is about $\sigma_n = 0.9$ N.m^{-1}, so the limit detection is chosen such as $\Delta S > 5 \times \sigma_n$ for all the experiments. Thus, the criterion used is $\Delta S_{min} = 5$ N.m^{-1} to detect an abnormal contact stiffness evolution (jump).

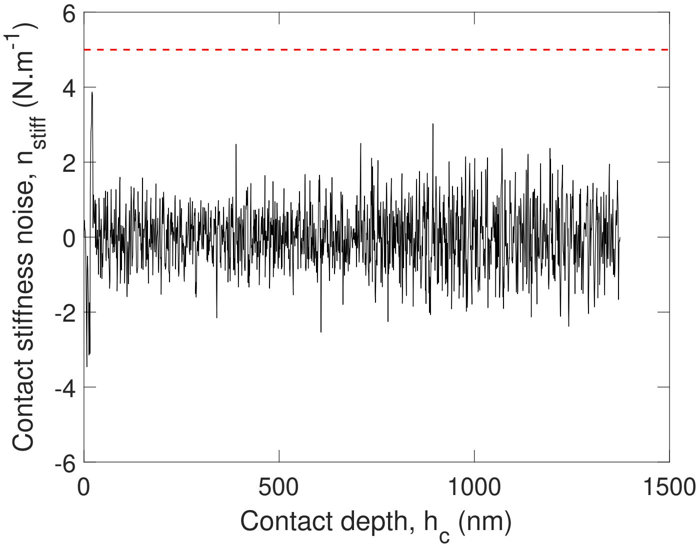

Figure 6: Evolution of stiffness around the general trend calculated by a moving average on 18 points.

3.2 Image analysis

The objective of the image analysis is to distinguish the carbon black aggregates from the fluoroelastomer and silicon matrix. Figure 7a displays the Transmission Electron Microscopy (TEM) observation of the elastomer in gray-scale. An image analysis post-treatment, described in more details in the appendix, is applied to the latter to obtain figure 7b which represents the binary matrix. Black zones are aggregates with logical a value of 0 and the white zone is the fluoroelastomer matrix with a logical value of 1. For this image, the side of one pixel is $e = 20.67$ nm.

3.3 Characterization of heterogeneities

3.3.1 From experimental data

The characterization of the jumps is performed based on the hypothesis of a constant material's modulus – i.e. fluoroelastomer matrix and silicon nanoparticles. This equivalent modulus is measured directly via CSM nanoindentation at depth greater than 1800 nm, in order to neglect the heterogeneities. Therefore the modulus used in the following develop-

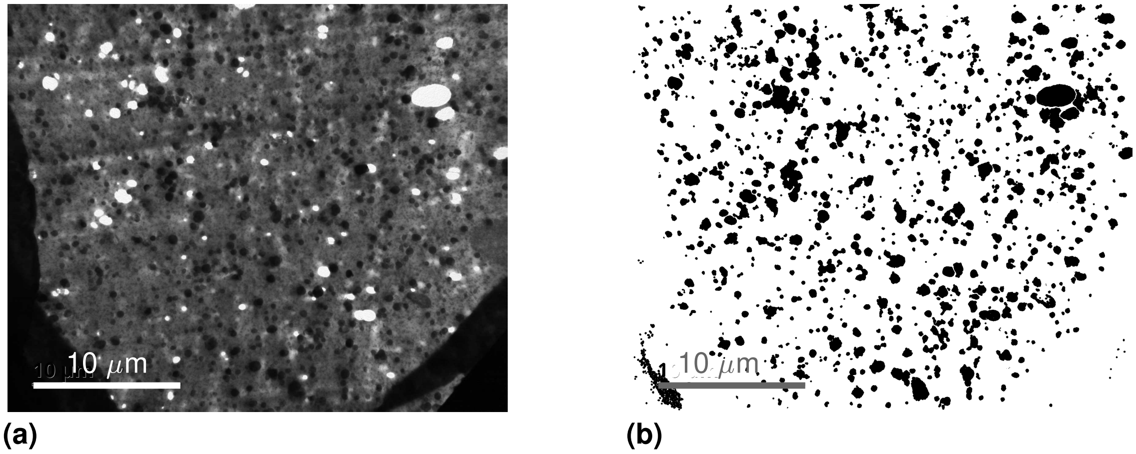

Figure 7: Isolation of the carbon black aggregates from the elastomer matrix by image analysis. (a) original TEM observation and (b) image analysis result, with the black particles corresponding to carbon black aggregates and the white part corresponding to the elastomer matrix.

ment is not directly the one of the fluoroelastomer and silicon matrix since the addition of carbon black aggregates must somehow increase the stiffness of the whole material.[2] Nevertheless, the use of this equivalent modulus remains a good approximation of the matrix behavior and allows the proposed method to be self sustaining. The reduced contact modulus measured is $E_c'^{*} = 39.5 \pm 5.4$ MPa. This value is significantly higher than the modulus E' measured by DMA – $E' = 15$ MPa – since the solicitation frequencies are 75 Hz for CSM and 1 Hz for DMA.

The contact stiffness signal is transformed into virtual contact depth h_{stiff} via the following equation:

$$h_{stiff} = \frac{tan(\beta) S}{2 E_c'^{*}} \tag{10}$$

If the material is homogeneous the expression of h_{stiff} versus h_c leads to an affine function with a slope of 1. However, in the case of a heterogeneous material, this curve will present varying slopes depending on the variation of stiffness with penetration depth.

Hence, every slope greater than 1 should represent a case where the contact stiffness is higher than it should be – i.e. an aggregate enters in contact with the tip – or lower than 1 – i.e. the contact between the aggregate and the tip is well established so the increase of contact area due to the penetration depth increase is less than it should be. The first criterion applied to detect a jump is the condition $\frac{dh_{stiff}}{dh_c} > 1.05$.

Another important criterion is the minimum stiffness detection ΔS_{min}, introduced in section 3.1, which states on representativeness of the detected jump compared to the measurement noise. All the numerical treatments leading to a correct detection of the jumps are given in the appendix.

Figure 8.a displays an example of a contact stiffness versus contact depth curve with its corresponding jumps highlighted by pairs of colored dots.

3.3.2 From model data

For the tip-particle numerical model, the stiffness of the contact S is estimated by equation 1 with $E_c'^*$ equal to 39.5 MPa and A_c the projected contact area as determined by image analysis. By knowing S, the virtual contact depth h_{stiff} is calculated with equation 10 and a similar analysis as for experimental data is performed. In this case, however, the criterion $\frac{dh_{stiff}}{dh_c} > 1.20$ is used because of numerical noise coming from pixel transformation during the simulation. All the numerical treatments leading to a correct detection of the jumps are given in the appendix.

The corresponding detection is illustrated in figure 8.b.

3.4 Estimation of particles area from numerical simulation

Figure 9 displays the ratio of indenter perimeter in contact with particles p_{part} over the total perimeter p_{tot}, as a function of the virtual contact depth. This ratio is related to the portion of one jump attributable to a new particle such as $\xi = (p_{tot} - p_{part})/p_{tot}$.

These values are calculated for 9 virtual indents. The error bars represents the mean values and the standard deviations calculated on a range of 100 nm for all the curves. The

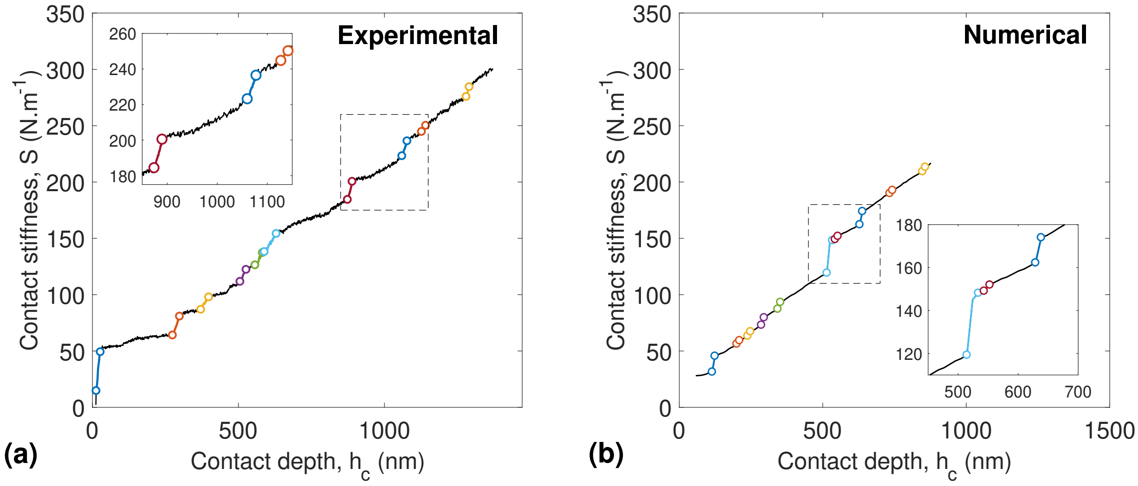

Figure 8: Evolution of contact stiffness with penetration depth from (a) experimental and (b) numerical simulation based on TEM observations. Jumps detection is highlighted by pair of dots.

ratio varies from zero to 0.6 as a function of indent's location and penetration depth. Thus it makes the attribution of a constant ξ value difficult. However, this ratio rarely exceeds 0.4 and lies principally around 0.2. This means that, between this material and a Berkovich tip, the average portion of tip perimeter in contact with particles is 20 %. So, the most probable value of ξ is 80 %.

In the following results, a value of $\xi = 0.8$ is used to approach the particles' projected area distribution.

It must be noted that this approach can be used for any kinds of particles shapes. Yet, values and evolution of ξ are highly sensitive to the particles' shapes and distributions. Therefore, this parameter is material dependent.

3.5 Distribution of particles area from numerical simulation

Figures 10 displays the distributions of particle surface density by range of 0.15 μm^2, in a 40×30 μm^2 slab of material. This distribution is calculated from the number of particles of a given projected area N_{expe} and from the total probed area:

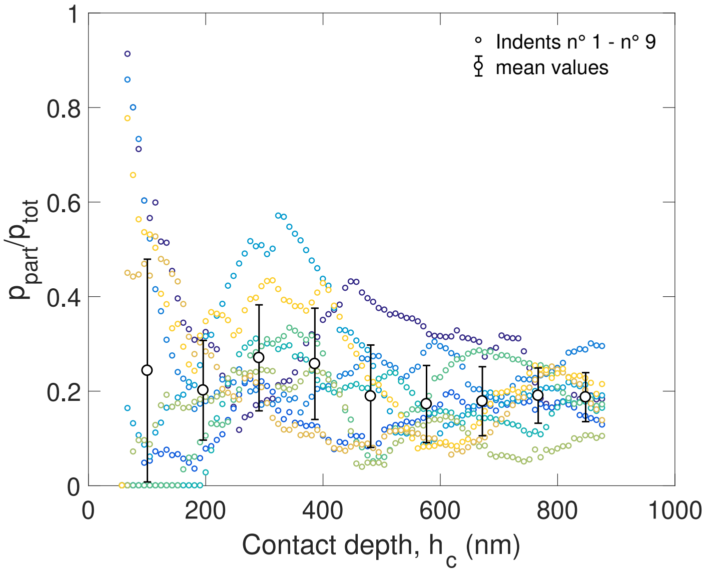

Figure 9: Ratio of indenter perimeter corresponding to particles over the total perimeter, as a function of contact depth, for 9 virtual indents.

$$D(A_{part}) = \frac{N_{exp}(A_{part})}{A_{probe}} \tag{11}$$

Where A_{probe} is the sum of the indentation projected areas at the end of loading, in the tip-particle model framework. This value depends on the number of numerical increments which is fixed during the simulation.

Table 1 provides the probing parameters used to characterize the particle surface density distributions. h_c is calculated at the end of the numerical loading with equation 13 defined in the appendix. This value depends also on the number of numerical increments. S_{max} is the average value – with standard deviation – of the maximum stiffness attained during each numerical simulation. Figures 10.a, .b and .c represent the calculated distributions for 9, 16 and 25 indents, respectively, with $\xi = 0.8$.

For all the cases, the tip-particle model tends to greatly underestimate occurrences of small particles, as expected from the expression 8. By varying both maximum stiffness S_{max} and minimum stiffness detection ΔS_{min}, a clear evolution of the minimum detectable particle size $\Delta A_{c,\ lim}$ is highlighted. Indeed, by decreasing the maximum stiffness S_{max}

Table 1: Probing parameters for characterization of particle surface density distribution

Distrib. Charac.	S_{max} (N.m^{-1})	h_c (nm)	A_{probe} (μm^2)
TEM	/	/	450
9 indents	204 ± 6	876	170
16 indents	159 ± 7	686	185
25 indents	101 ± 10	410	103

while keeping the minimum stiffness detection ΔS_{min} constant, the characterization of small particles distribution is enhanced. Furthermore, the same conclusion can be drawn if ΔS_{min} is decreased while keeping S_{max} constant. In other terms, the best way to detect the broadest range of particle sizes is to perform the smallest indentation feasible.

3.6 Application to experimental indentation testing

Figure 11 displays the distributions of particles surface density by range of 0.45 μm^2, in a 40×30 μm^2 slab of material. The probed areas A_{probe} are sensibly the same for the TEM observation and the experimental data ($A_{probe} \approx 450$ μm^2). In this case, the minimum particle size fully detected is $\Delta A_{c,\ lim} = 1.46$ μm^2. The best detection threshold for our experimental set-up would allow to attain $\Delta A_{c,\ lim} = 0.50$ μm^2 with a maximum stiffness $S_{max} = 100$ N.m^{-1}. The effect of the stiffness instability's portion attributed to a particle, ξ, on the distribution calculation is highlighted on figure 11 where the two extremes cases are displayed. As it has been said in previous section, considering $\xi = 0$ leads to systematic overestimation of the measured particles' area A_{part}. Hence, the distribution of particle surface density is translated to higher particles' area. The contrary remark is valid for $\xi = 1$, which is not obvious in figure 11 since other sources of particles' area A_{part} overestimation are present. The latter will be explain is the following paragraphs.

Figure 12 highlights the influence of measured matrix's reduced contact modulus on the distributions calculations. It displays the distributions of particles surface density by range

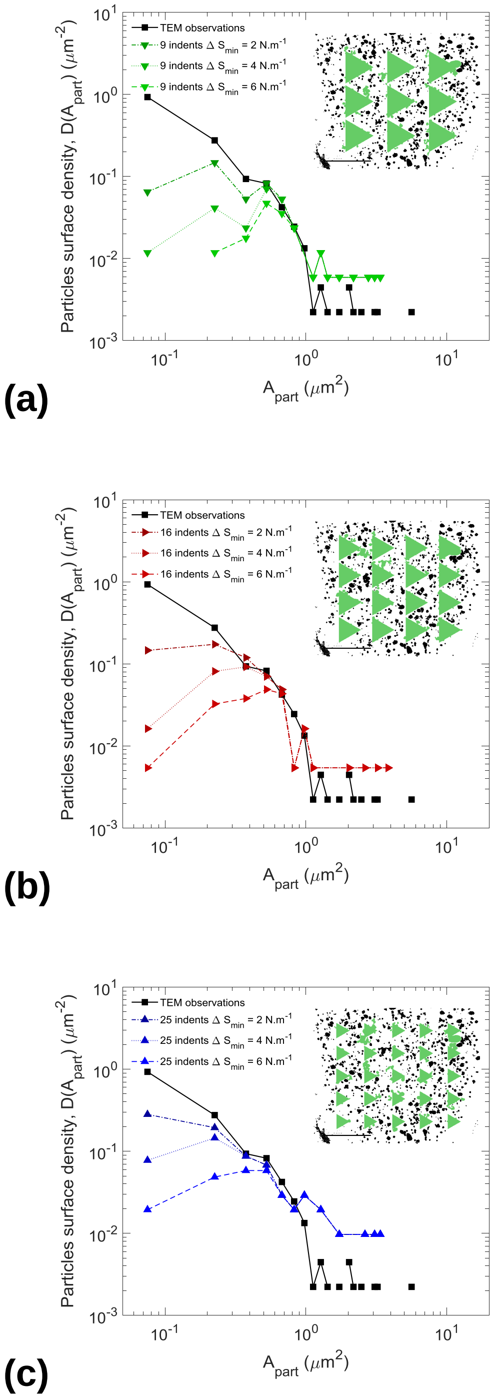

Figure 10: Particles surface density, characterized by image analysis and the tip-particle model with (a) 9 indents, (b) 16 indents and (c) 25 indents. The number of occurrences of a certain particle size is divided by the total probed area – i.e. contact area at maximum depth for indentation data.

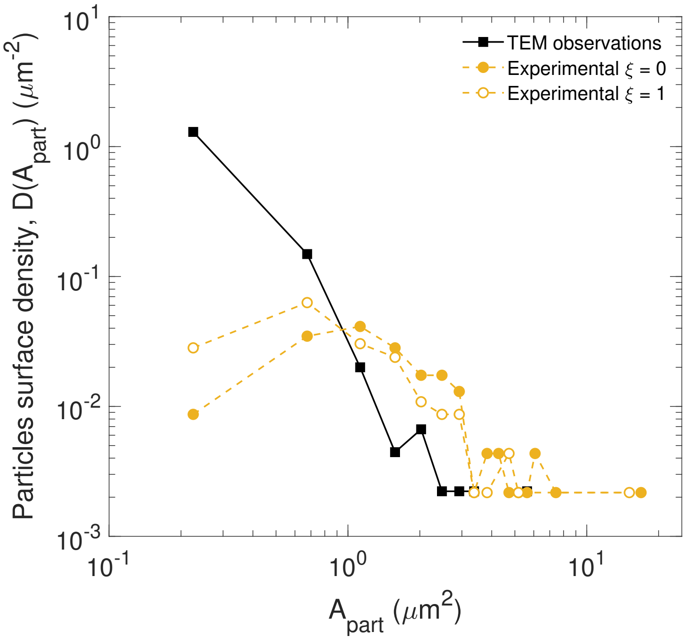

Figure 11: Particles surface density, characterized by image analysis for TEM observations and experimentally from the tip-particle model and experimental curves calculated with different level of correction – i.e. $\xi = 0$ and $\xi = 1$.

of 0.45 μm^2, in a 40×30 μm^2 slab of material for the same set of experiments.

These distributions are calculated from experimental tests by the tip-particle model with a minimum stiffness detection, $\Delta S_{min} = 5$ N.m^{-1} and $\xi = 0.8$, in yellow and the distribution calculated from TEM observation in black. The three experimental distributions are calculated with the same set of indentation tests with different reduced contact moduli $E_c'^*$. The plain circle symbols correspond to the mean value of $E_c'^*$ and the up-pointing and down-pointing triangles correspond to the standard deviations of the reduced contact modulus, respectively. The choice of the modulus affects the calculation of the distribution such as, for higher modulus the calculated areas of the particles are smaller, see figure 12. This leads to an overestimation of the small particles' surface density and an underestimation of the large particles' surface density. In the other hand, if a lower modulus is taken to represent the matrix, the calculated areas of the particles would be higher.

As for numerical simulation results, the surface density of small particles – i.e. $A_{part} \leq$ 0.375 μm^2 – is greatly underestimated whatever the reduced contact modulus taken into

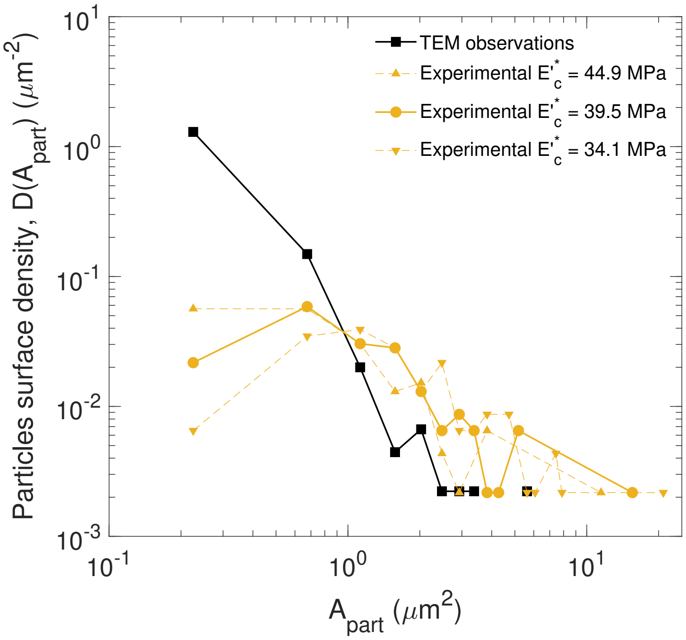

Figure 12: Particles surface density, characterized by image analysis for TEM observations and experimentally from the tip-particle model and experimental curves calculated with different reduced contact moduli – mean value and standard deviation values.

account. This is due to the model limitations, as explained previously.

Also, the distribution of larger particles is well above the one measured via TEM observations. Here again a parallel can be drawn with the numerical simulations results which indicates that the overestimation of large particles – i.e. $\Delta A_c > 0.525$ μm^2 – is enhanced by the increase of the indent size. This behavior is related to the indent perimeter and highlights the fact that multiple "small" particles can enter in contact nearly simultaneously with the tip and act as a "large" particle on the measured stiffness. Therefore, the longer the indent perimeter, the higher the probability to detect several particles in the same stiffness instability.

However, this explanation is not sufficient to describe the difference between the experimental particles surface density distribution and the TEM observations. In the case of the TEM observations, the material is assumed to be in two dimensions – the thickness of the sample being around 100 nm – contrary to the experimental set-up where the sample is considered with 3 dimensions. Thus, increasing the indentation size enhances the contributions of deep particles to the measured contact stiffness. The term "surface density" as to be employed with care when the indentation depth is significantly greater than the particles size.

3.7 Correction of the measured distributions

The tip-particle model reliability has been investigate through numerical and experimental analyses and give access to a correct particle distribution within the model hypotheses. In this paragraph, the proposed correction (equation 9) derived from the tip-particle model is applied to the numerical and experimental particle distributions.

Figure 13 displays the corrected numerical distributions calculated from the same data set as figure 10, with average values of S_{max} from Table 1 and different values of ΔS_{min} as shown in Figure 13. An excellent agreement between the TEM observation and the corrected distributions is shown, whatever the tested conditions – i.e. various ΔS_{min} and S_{max}. Even if the tested conditions have an effect on the result and must be chosen with care, it is very pleasant to see that a unique solution can be extracted from the stiffness measurement.

Figure 14 displays the corrected distributions of particle surface density $D(A_{part})$ calculated in the same conditions as in figure 12. These distributions are calculated from experimental tests by the tip-particle model with a minimum stiffness detection, $\Delta S_{min} = 5$ N.m^{-1}, an average maximum stiffness, $S_{max} = 310 \pm 49$ N.m^{-1}, a reduced contact modulus $E_c'^{*} = 39.5\ GPa$ and $\xi = 0.8$. The as-measured distribution is represented with circle symbols, the corrected one is represented with diamond symbols and the one calculated from TEM observation with square symbols. Here again, the agreement between the TEM distribution and the corrected experimental one is reasonable, taking into account the relatively unfavorable tested conditions.

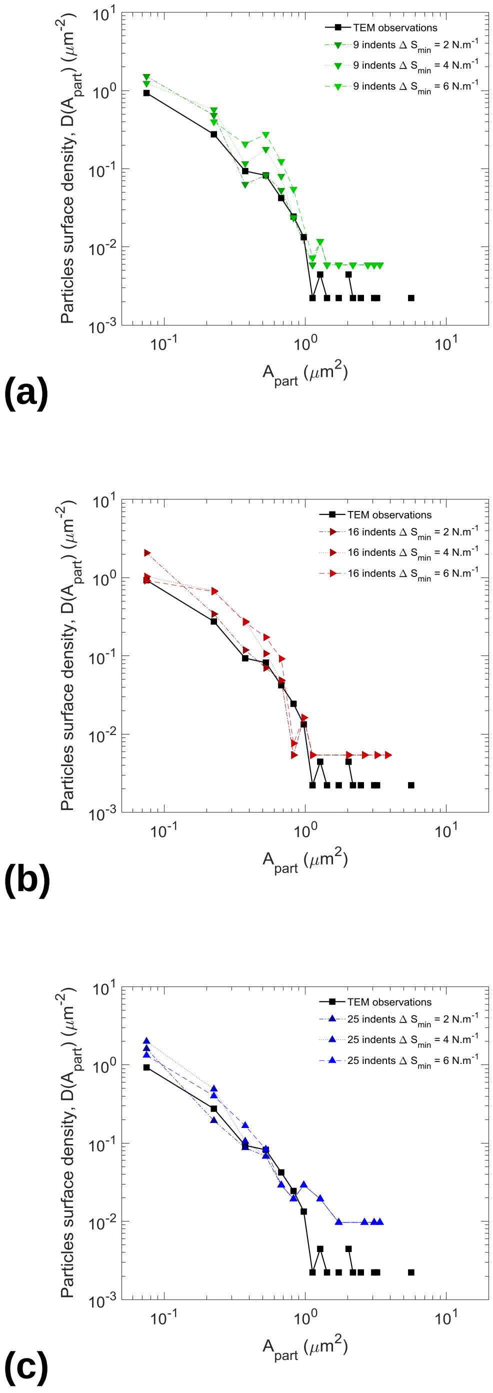

Figure 13: Particles surface density, characterized by image analysis and the tip-particle model corrected from the measurement bias α_{equ} with (a) 9 indents, (b) 16 indents and (c) 25 indents. The number of occurrences of a certain particle size is divided by the total probed area – i.e. contact area at maximum depth for indentation data.

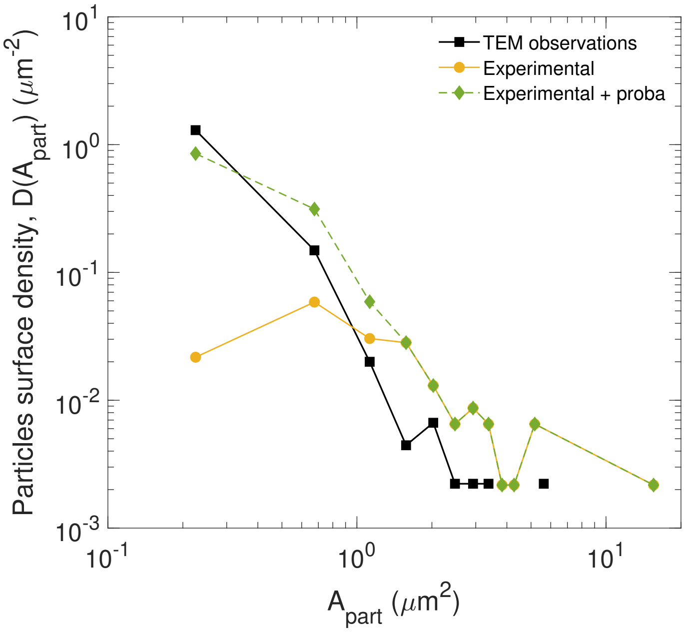

Figure 14: Particles surface density, characterized by image analysis for TEM observations and from the tip-particle model corrected from the measurement bias α_{equ}.

3.8 Tip-particle model limitations

The tip-particle model has been investigated numerically in order to better understand its limitations. We have seen in section 3.7 that the main source of error arises from the loading limitation. This is promising since the measurement bias is expressed by equation 8 which is only a function of experimental inputs ΔS_{min} and S_{max}.

However, some deviations are not due to loading considerations and should come from these model limitations :

- The model tends to overestimate the size of the detected particles since the indenter can enter in contact with several particles at the same time. This configuration is highlighted on figure 15.a where the particles 2 and 3 enter in contact successively with the virtual indent. Figure 15.b displays the corresponding evolution of stiffness with contact depth and one can see that the two particles are detected as one jump. This issue is getting more and more probable as the contact perimeter between the tip and the material increases. Thus, the smaller the indent the less probable the detection

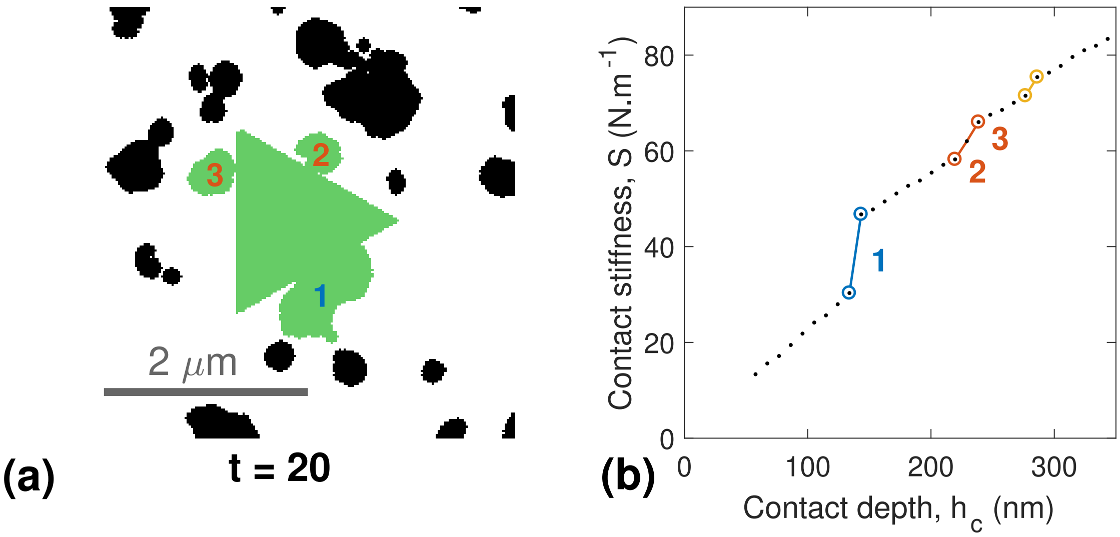

Figure 15: Numerical simulation of indentation applied on the binary image extracted from TEM observation: (a) increments $t = 19$ and $t = 20$ the virtual indenter enters in contact with two particles successively ; (b) contact stiffness evolution with contact depth and detection of the stiffness jump.

of several particles at once.

- Only particles in the near surface participate to the tip-particle extension. Indeed, the particles need to be in direct contact in order to play the role of tip's hard extensions. However, with increasing penetration, the elastomer matrix between the particles is more and more confined. Therefore, the participation of deeper particles to the total projected area is enhanced. This also leads to an overestimation of the particles sizes.

- Furthermore, if particles are too close to each other, the tip-particle extension will not allow to isolate the contribution of particles independently.

- Particles are sometimes hidden by a bigger one contacting the tip previously. Hence, the contact stiffness is much higher than in the homogeneous case and the addition of a small area may not be sufficient to generate a stiffness jump greater than the minimum detection limit ΔS_{min}. In such case, the particle is not detected and the particle surface density for the concerned range of particle area is underestimated.

4 Conclusions

In the framework of highly heterogeneous materials, a new method to characterize the local distribution of particles surface density is proposed. The latter applies to materials presenting high mechanical properties contrast between its different phases. In this study, particles are stiffer and harder by a factor of 100 compared to the fluoroelastomer matrix. Further investigations may address the lower limit of these mechanical properties contrasts.

An extensive study of the tip-particle extension is provided based on numerical and experimental approaches. Therefore, the main conclusions are:

- Quantitative distribution of particles surface density can be measured from stiffness jumps during nanoindentation loading.
- Accuracy of the measured particles' surface density distributions depends on the minimum detectable stiffness jump and the maximum load applied.
- The higher the number of indentation, the more accurate the measured distribution.
- An analytical correction based on experimental parameters can be applied to account for the smallest particles that might have been miscounted.

Nanoindentation testing appears eventually as an interesting alternative to Transmission Electron Microscopy to measure hard nanoparticles local distribution in an elastomer matrix.

Acknowledgement

This work was supported by the LABEX MANUTECH-SISE (ANR-10-LABX-0075) of Université de Lyon within the program "Investissements d'Avenir" (ANR-11-IDEX-0007) operated by the French National Agency (ANR). The authors thank also the financial support from Institut Carnot Ingénierie@Lyon and Institut Carnot M.I.N.E.S.

Appendix

Image analysis

The following treatment steps are applied to the image:

- The gray-scale image is transformed into a logical matrix by mean of an adaptive threshold algorithm available on Matlab®. The threshold value is modified as a function of the neighbors pixel mean intensity. The matrix obtained is named B_1.
- A morphological operation is then applied to isolate the particles' representative elements by specifying a minimum aggregate radius. The matrix B is obtained from $B1$.
- As it can be seen on the figure 1, some particles are white. Those elements correspond to aggregates that have been removed from the TEM "blade" during their preparation. As a consequence, another adaptive threshold algorithm is applied to isolate them from the matrix and obtain a matrix named C.
- The matrix containing all the aggregates is then written as $D = B + \bar{C}$. Then, the irrelevant pixel groups are removed such as only particles greater than 45 pixels remain. This matrix is represented on the figure 7.b.

Jump detection

From experimental data

The post-treatment steps aim at isolating the segments characterized as stiffness jumps:

1. First, an equivalent contact depth h_{stiff} is calculated, with the hypothesis of a constant and homogeneous reduced contact modulus $E_c'^*$, from equation 10. It is done to normalize the stiffness signal according to the contact depth and allows for a simple criterion to be set: $\frac{dh_{stiff}}{dh_c} > 1.05$ is equivalent to a jump.

2. In a second step, a sampling at a constant frequency of displacement is performed. Originally, the acquisition frequency is fixed at 5 Hz, but since the loading procedure is exponential according to time, the interval between two consecutive penetration depths increases with time. The sampling is performed in order to get a 0.8 nm spacing between the data which is in the same order of magnitude as the intervals during all the loading procedure – i.e. 0.4 to 3 nm.

3. Following this step, a numerical derivative is performed by fitting an affine function on 18 points around the concerned contact displacement value. Hence, a moving derivative is obtained. An example of the resulting treatment is presented on figure 16.a.

4. This numerical derivative is then compared to the limit detection which is fixed at $\frac{dh_{stiff}}{dh_c} > 1.05$, as illustrated by the dashed red line on figure 16.a.

5. An evaluation of the fit goodness is performed with the criterion R^2 for each calculated derivative. A segment is considered as a **potential jump** when the criterion 4 is fulfilled together with $R^2 > 0.8$ and segment length superior to 1 point, as shown in figure 16.b with the dashed red line.

6. Then, each segments satisfying criterion 5 is tested with the conditions $R^2 > 0.9$, as shown in figure 16.b with the dashed blue line. If, at least, one fit satisfies this condition in the concerned segment, it is still considered as a **potential jump** segment. The red arrows in figure 16.b represent two cases where $R^2 < 0.9$ in the segments, which means that the slope calculated here is not relevant. Indeed, in figure 16.c it is difficult to assess the presence of a jump in the two concerned areas.

7. Finally, each segment stiffness amplitude is calculated and only $\Delta S > \Delta S_{min}$ are considered as real particles. ΔS_{min} is 5 N.m^{-1} in our study.

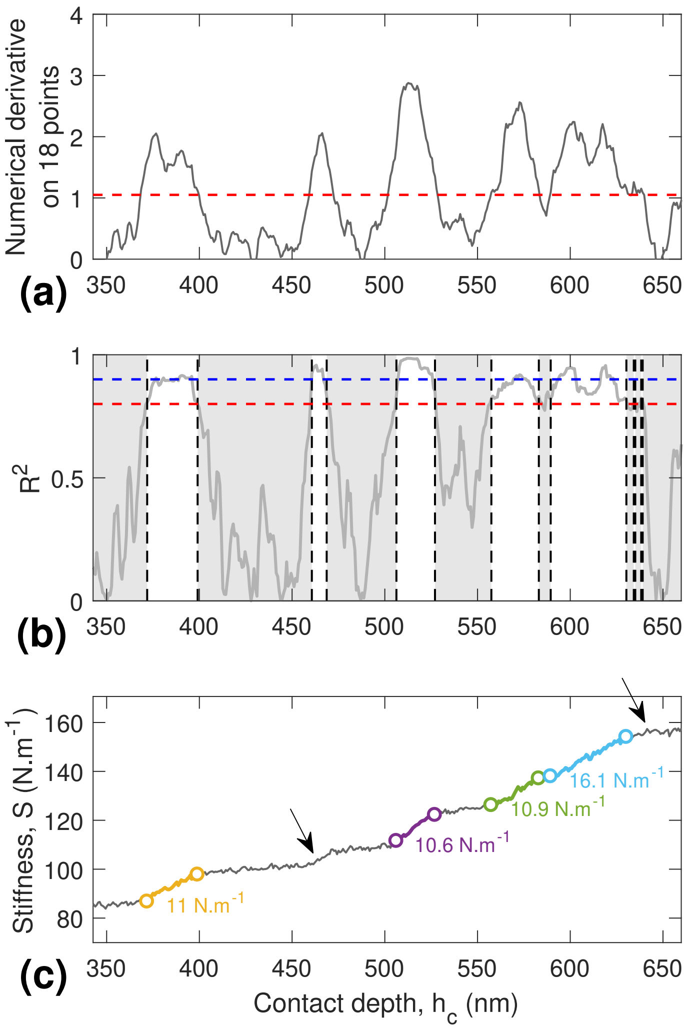

Figure 16: Detection of "jump" segments: (a) Moving derivative of the curve h_{stiff} *vs.* h_c on 20 points, the red dashed line describes the condition necessary to consider a jump $dh_{stiff}/dh_c > 1.05$ ($C1$); (b) coefficients of goodness R^2 for the fitted derivative (a), gray bands highlight the segments that do not fulfill the condition $R^2 > 0.8$ ($C2$), described by the dashed red line, during enough data points. The blue dashed line describes the other condition to be fulfill $R^2 > 0.9$ ($C3$), the two red arrows point out the state $C1 = 1$ & $C2 = 1$ & $C3 = 0$; (c) if all the conditions of figure (a) and (b) are completed, the jump segment is defined by the colored dots pairs.

From model data

The numerical model is based on the comparison of the image analysis performed on the TEM observation and several virtual indents. Figure 17 represents a numerical indent at two different simulation increments. On figure 17.a, the virtual indent lies completely in the fluoroelastomer matrix and on figure 17.b the virtual indent touches a particle. The area of contact is displayed in light green.

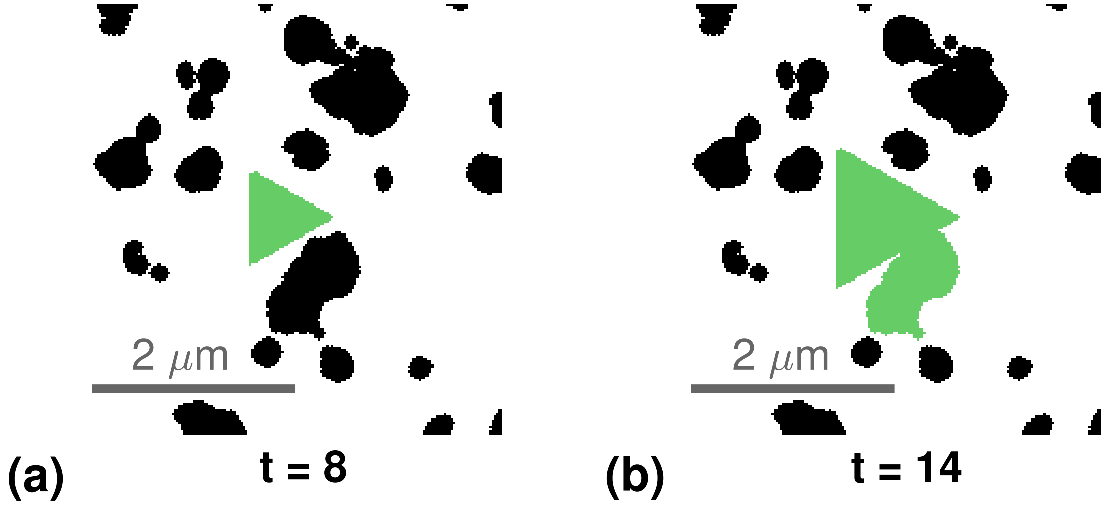

Figure 17: Numerical simulation of indentation applied on the binary image extracted for TEM observation: (a) increment $t = 8$, the virtual indenter lies on the fluoroelastomer matrix ; (b) increment $t = 14$ the virtual indenter is in contact with particle 1.

Hence, at each simulation step, the pixels corresponding to the three sides of the equilateral triangle are calculated and written as vectors noted ($\vec{L_i}(t) = [X_i(t), Y_i(t)]$). From the three vectors, the triangle is computed and the corresponding pixels in the area are set at logical value of 1, all the other pixels of the matrix are set to 0. This indenter matrix is named E_t with t the increment. Then, the matrix E_t containing the triangle is superposed on the image analysis matrix D such as $F_t = \bar{D}.E_t$. From this resulting matrix, the area of the zone with logical value 1 and containing the initial barycenter of the triangle is registered. The area evolution is calculated by the number of pixels multiplied by the equivalent surface of a pixel such as $A_c(t) = N_{pix}(t)e^2$ and then stiffness and contact depth can be calculated with following equations:

$$S(t) = 2E_c'^* \sqrt{\frac{A_c(t)}{\pi}} \qquad (12)$$

$$h_c(t) = e\big(||\vec{L}_i(1)|| + 2(t-1)\tan(60)\big)\frac{\sqrt{3}}{6\tan(65.27)} \tag{13}$$

With $||\vec{L}_i(1)||$ the length of one side of the equilateral triangle at increment 1. The angles are relative to the Berkovich geometry.

Finally, to evaluate the presence of stiffness jump the ratio between the virtual contact depth h_{stiff} (equation 10) and the contact depth h_c is calculated. The criterion $\frac{dh_{stiff}}{dh_c} > 1.20$ is applied to detect the stiffness instabilities. If this relation is false, the ratio is set to zero. The segments corresponding to jumps are then isolated and their stiffness amplitude ΔS are compared to the minimum stiffness detection ΔS_{min}. As for experimental treatment, only $\Delta S > \Delta S_{min}$ are kept.

References

(1) Bergström, J. S.; Boyce, M. C. Mechanical Behavior of Particle Filled Elastomers. *Rubber Chemistry and Technology* **1999**, *72*, 633–656.

(2) Bentoumi, M.; Mdarhri, A.; Montagne, A.; Nourdine, A.; El Aboudi, I.; Iost, A. Nanoindentation for Probing Mechanical Properties of Nanocomposites Based on Ethylene Butyl Acrylate Copolymer and Carbon Black. *Journal of Applied Polymer Science* **2019**, *136*, 47897–47904.

(3) Hardiman, M.; Vaughan, T.; McCarthy, C. The Effect of Microscale Residual Stress from Thermal Cooldown on the Nanoindentation Properties of Fibre-reinforced Composites. *Journal of Composite Materials* **2016**, *50*, 4147–4158.

(4) Douce, J.; Boilot, J.-P.; Biteau, J.; Scodellaro, L.; Jimenez, A. Effect of Filler Size and Surface Condition of Nano-sized Silica Particles in Polysiloxane Coatings. *Thin Solid Films* **2004**, *466*, 114–122.

(5) Mdarhri, A.; Brosseau, C.; Zaghrioui, M.; El Aboudi, I. Electronic Conduction and Microstructure in Polymer Composites Filled with Carbonaceous Particles. *Journal of Applied Physics* **2012**, *112*, 034118–034130.

(6) Robertson, C. G.; Lin, C. J.; Rackaitis, M.; Roland, C. M. Influence of Particle Size and Polymer-Filler Coupling on Viscoelastic Glass Transition of Particle-Reinforced Polymers. *Macromolecules* **2008**, *41*, 2727–2731.

(7) Améduri, B.; Boutevin, B.; Kostov, G. Fluoroelastomers: Synthesis, Properties and Applications. *Progress in Polymer Science (Oxford)* **2001**, *26*, 105–187.

(8) Koo, J. H. *Polymer Nanocomposites: Processing, Characterization, and Applications*; McGraw-Hill Education: New York, 2006.

(9) Berthier, D.; Deffarges, M.-P.; Berton, N.; Venin, M.; Lacroix, F.; Schmaltz, B.; Tendron, Y.; Pestel, E.; Tran-Van, F.; Méo, S. POSS Nanofiller-Induced Enhancement of the Thermomechanical Properties in a Fluoroelastomer Terpolymer. *Materials* **2018**, *11*, 1358–1374.

(10) Agbabiaka, A.; Wiltfong, M.; Park, C. Small Angle X-Ray Scattering Technique for the Particle Size Distribution of Nonporous Nanoparticles. *Journal of Nanoparticles* **2013**, *2013*, 1–11.

(11) Pyrz, W. D.; Buttrey, D. J. Particle Size Determination Using TEM: A Discussion of Image Acquisition and Analysis for the Novice Microscopist. *Langmuir* **2008**, *24*, 11350–11360.

(12) Wagner, J.; Härtl, W.; Hempelmann, R. Characterization of Monodisperse Colloidal Particles: Comparison between SAXS and DLS. *Langmuir* **2000**, *16*, 4080–4085.

(13) Koga, T.; Hashimoto, T.; Takenaka, M.; Aizawa, K.; Amino, N.; Nakamura, M.; Yamaguchi, D.; Koizumi, S. New Insight into Hierarchical Structures of Carbon Black

Dispersed in Polymer Matrices: A Combined Small-Angle Scattering Study. *Macromolecules* **2008**, *41*, 453–464.

(14) Thünemann, A. F.; Rolf, S.; Knappe, P.; Weidner, S. In Situ Analysis of a Bimodal Size Distribution of Superparamagnetic Nanoparticles. *Analytical Chemistry* **2009**, *81*, 296–301.

(15) Tscharnuter, W. *Encyclopedia of Analytical Chemistry*; John Wiley & Sons, Ltd: Chichester, UK, 2000; pp 1–16.

(16) Herrmann, V.; Unseld, K.; Fuchs, H.-B. The Scale Behavior of Fillers in Elastomers by means of Indentation Tests. *Colloid and Polymer Science* **2002**, *280*, 267–273.

(17) Jenei, I. Z.; Dassenoy, F.; Epicier, T.; Khajeh, A.; Martini, A.; Uy, D.; Ghaednia, H.; Gangopadhyay, A. Mechanical Characterization of Diesel Soot Nanoparticles: In Situ Compression in a Transmission Electron Microscope and Simulations. *Nanotechnology* **2018**, *29*, 085703–085715.

(18) Baral, P.; Guillonneau, G.; Kermouche, G.; Bergheau, J.-M.; Loubet, J.-L. Theoretical and Experimental Analysis of Indentation Relaxation Test. *Journal of Materials Research* **2017**, *32*, 2286–2296.

(19) Oliver, W. C.; Pharr, G. M. An Improved Technique for Determining Hardness and Elastic Modulus using Load and Displacement Sensing Indentation Experiments. *Journal of Materials Research* **1992**, *7*, 1564–1583.

(20) Syed Asif, S. a.; Pethica, J. B. Nanoindentation Creep of Single-Crystal Tungsten and Gallium Arsenide. *Philosophical Magazine A* **1997**, *76*, 1105–1118.

(21) Kermouche, G.; Loubet, J. L.; Bergheau, J. M. Extraction of Stress-Strain Curves of Elastic-Viscoplastic Solids using Conical/Pyramidal Indentation Testing with Application to Polymers. *Mechanics of Materials* **2008**, *40*, 271–283.

Graphical TOC Entry

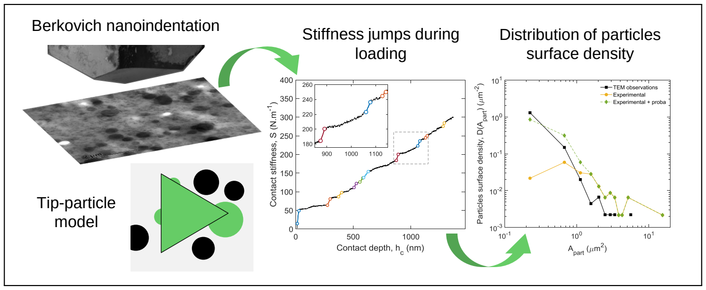

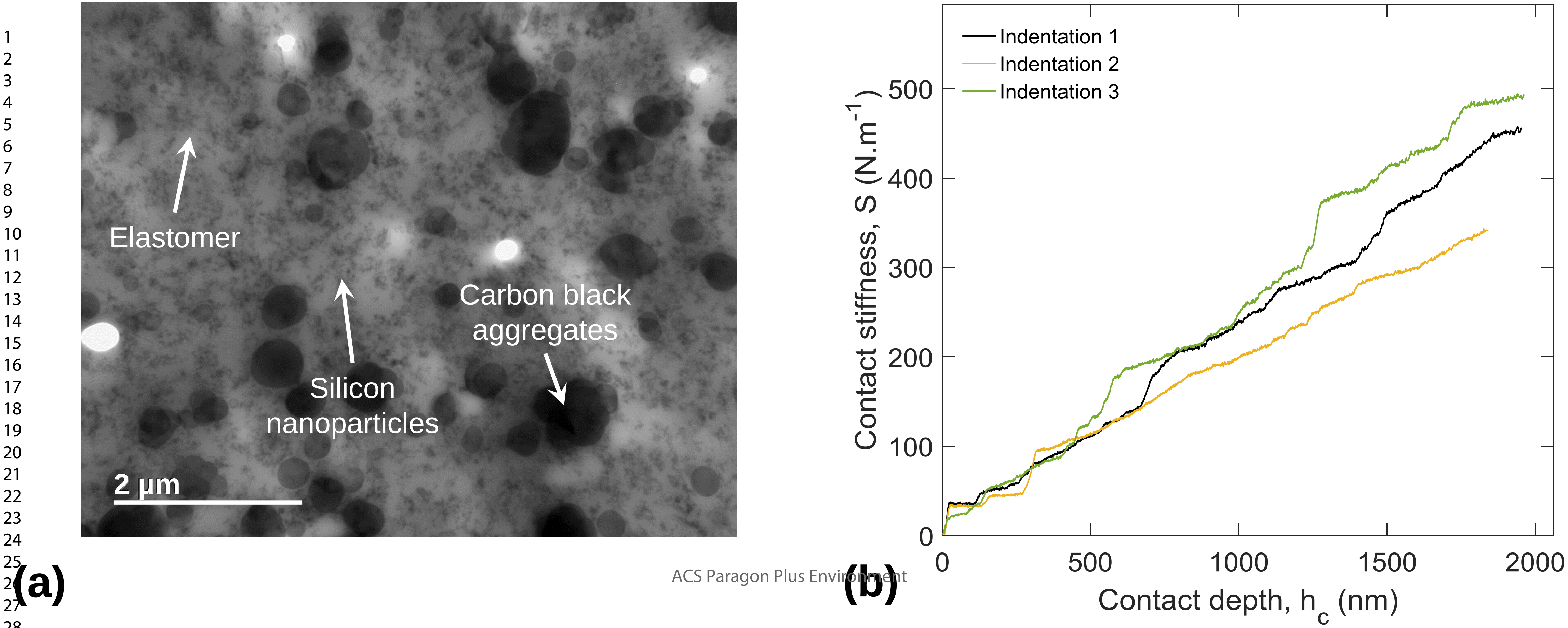
Elastomer
Silicon nanoparticles
Carbon black aggregates
2 µm
(a)
(b)
Indentation 1
Indentation 2
Indentation 3
Contact stiffness, S (N.m^{-1})
0
100
200
300
400
500
Contact depth, h_c (nm)
0
500
1000
1500
2000

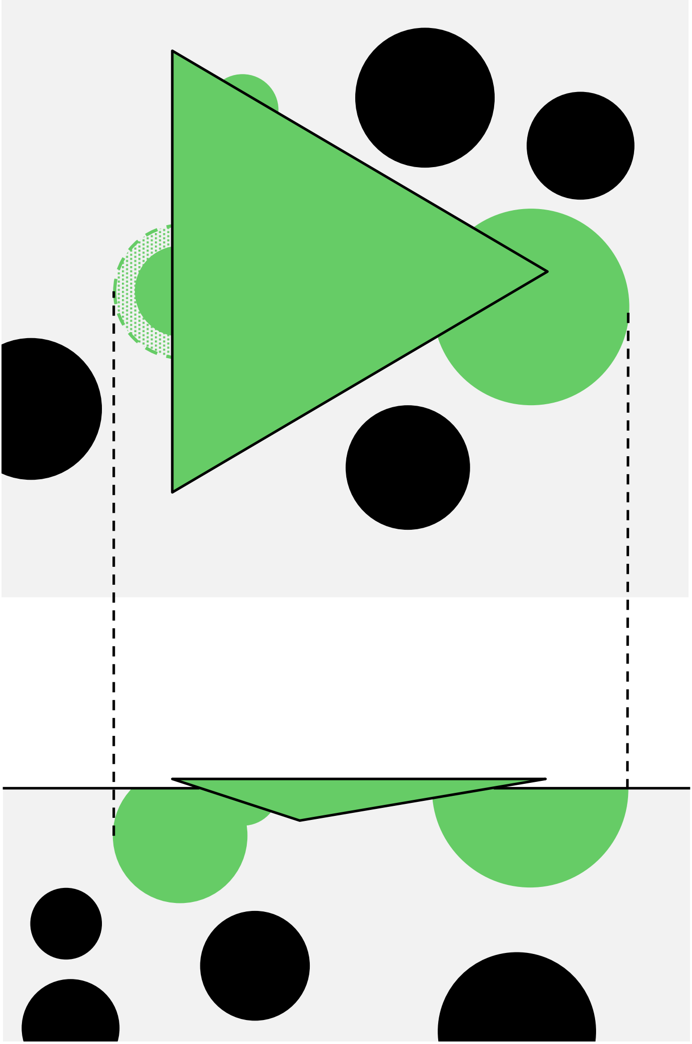

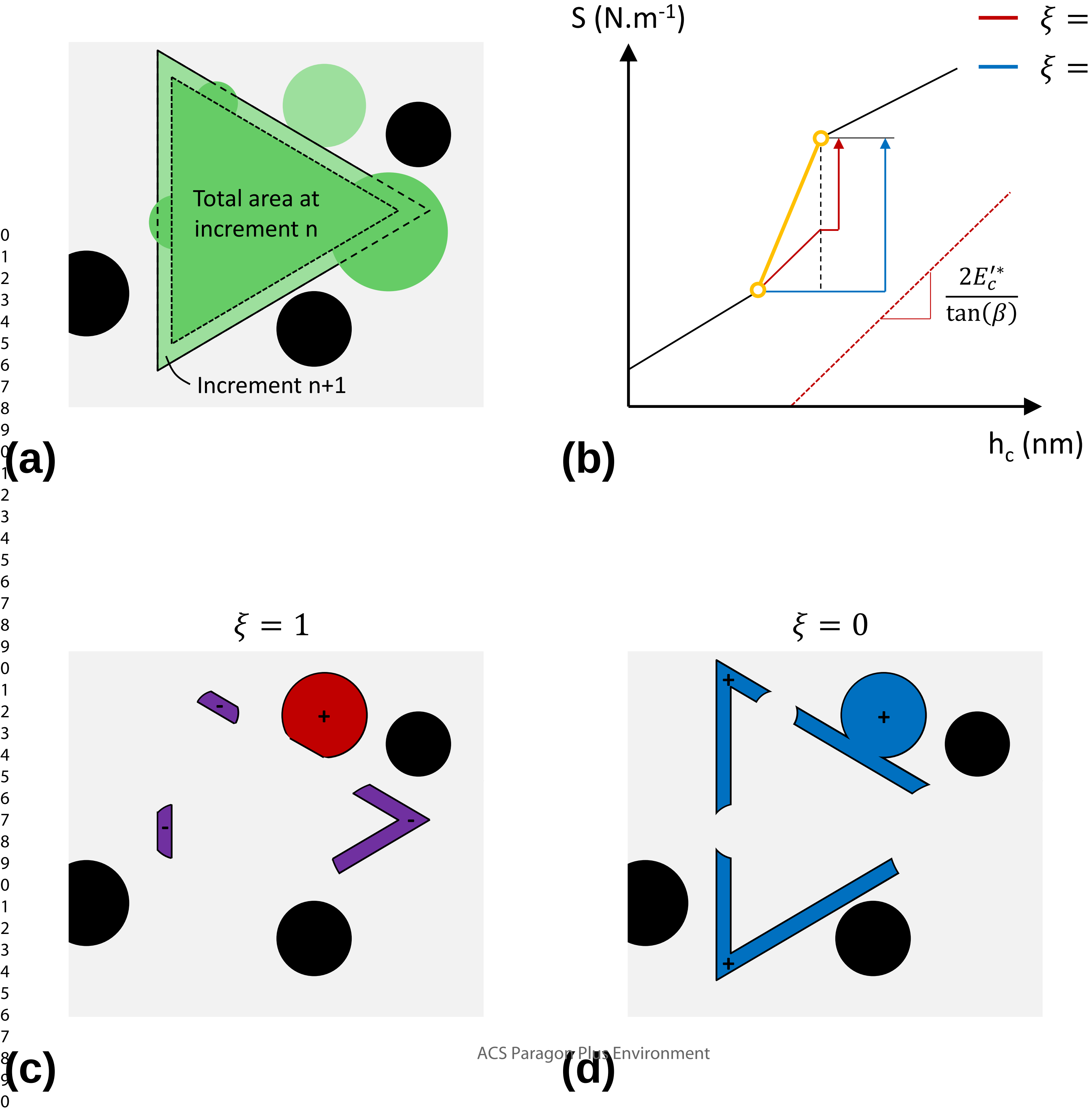
Total area at increment n
Increment n+1
(a)
S (N.m^{-1})
$\xi = 1$
$\xi = 0$
$\frac{2E_c'^*}{\tan(\beta)}$
h$_c$ (nm)
(b)
$\xi = 1$
+
-
-
-
(c)
$\xi = 0$
+
+
+
(d)

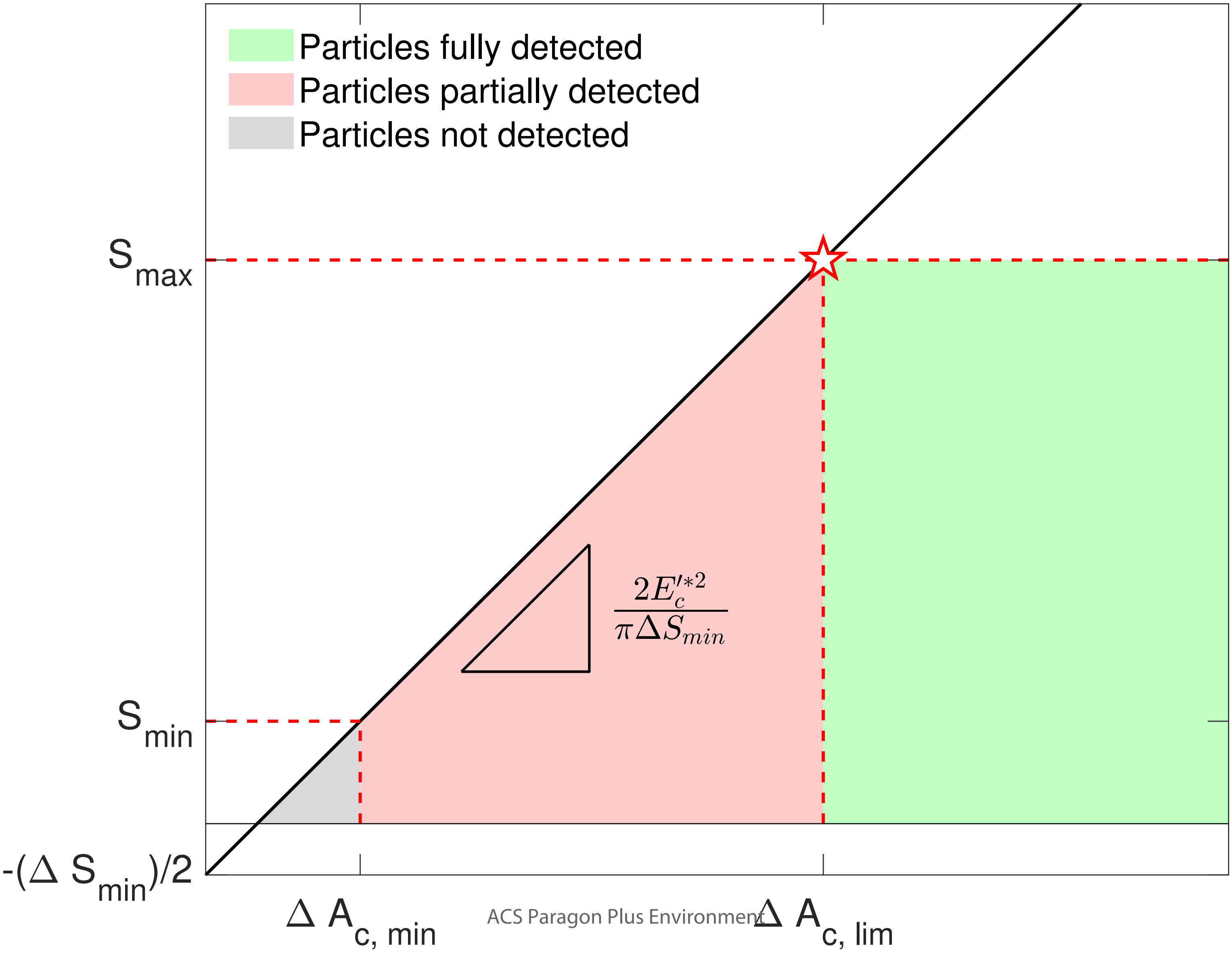
Particles fully detected
Particles partially detected
Particles not detected
S_{max}
S_{min}
$-(\Delta S_{min})/2$
$\frac{2E_c'^{*2}}{\pi \Delta S_{min}}$
$\Delta A_{c,\,min}$
$\Delta A_{c,\,lim}$

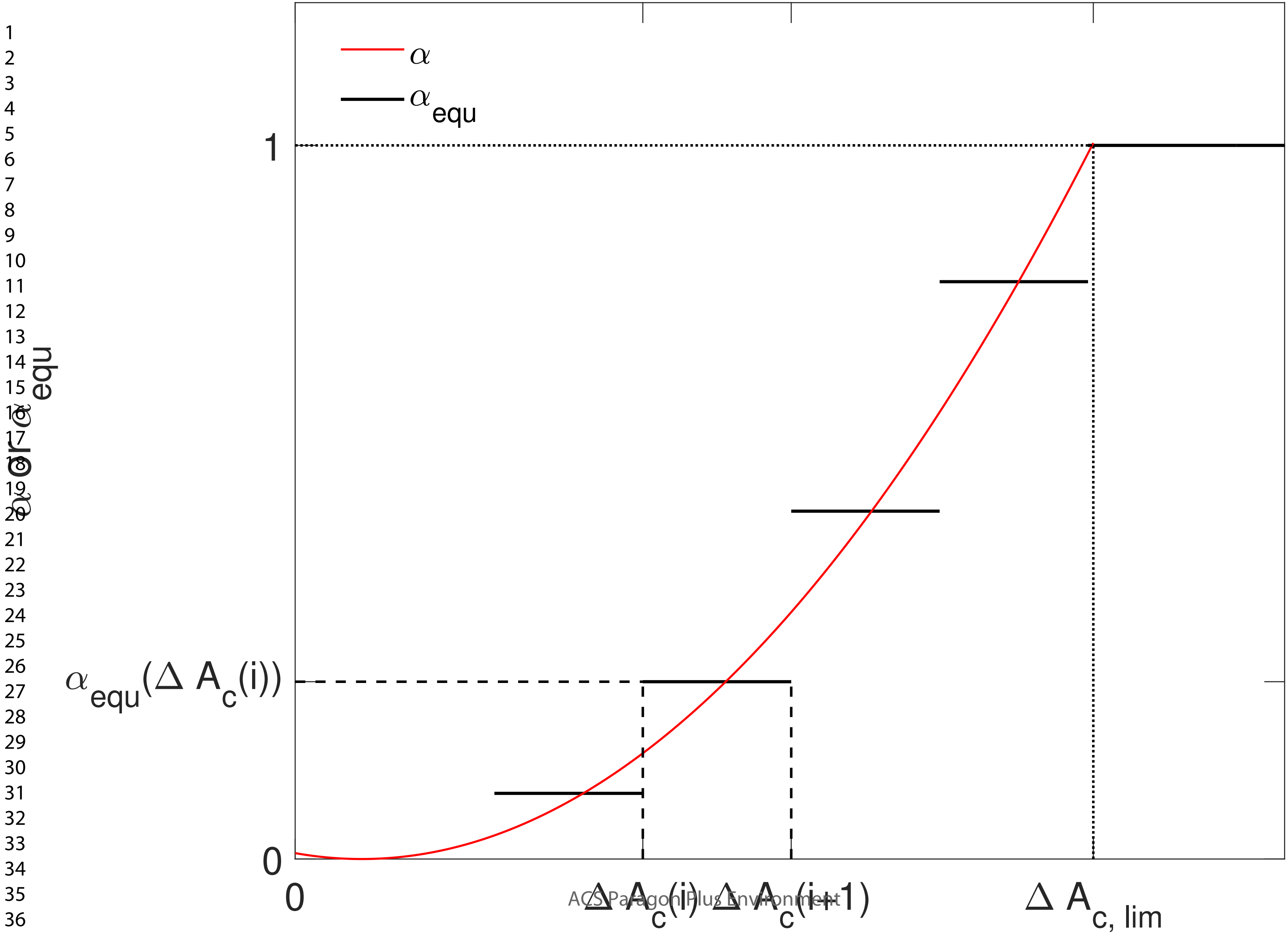
α
α_{equ}
1
0
α or α_{equ}
$\alpha_{equ}(\Delta A_c(i))$
0
$\Delta A_c(i)$
$\Delta A_c(i+1)$
$\Delta A_{c, lim}$

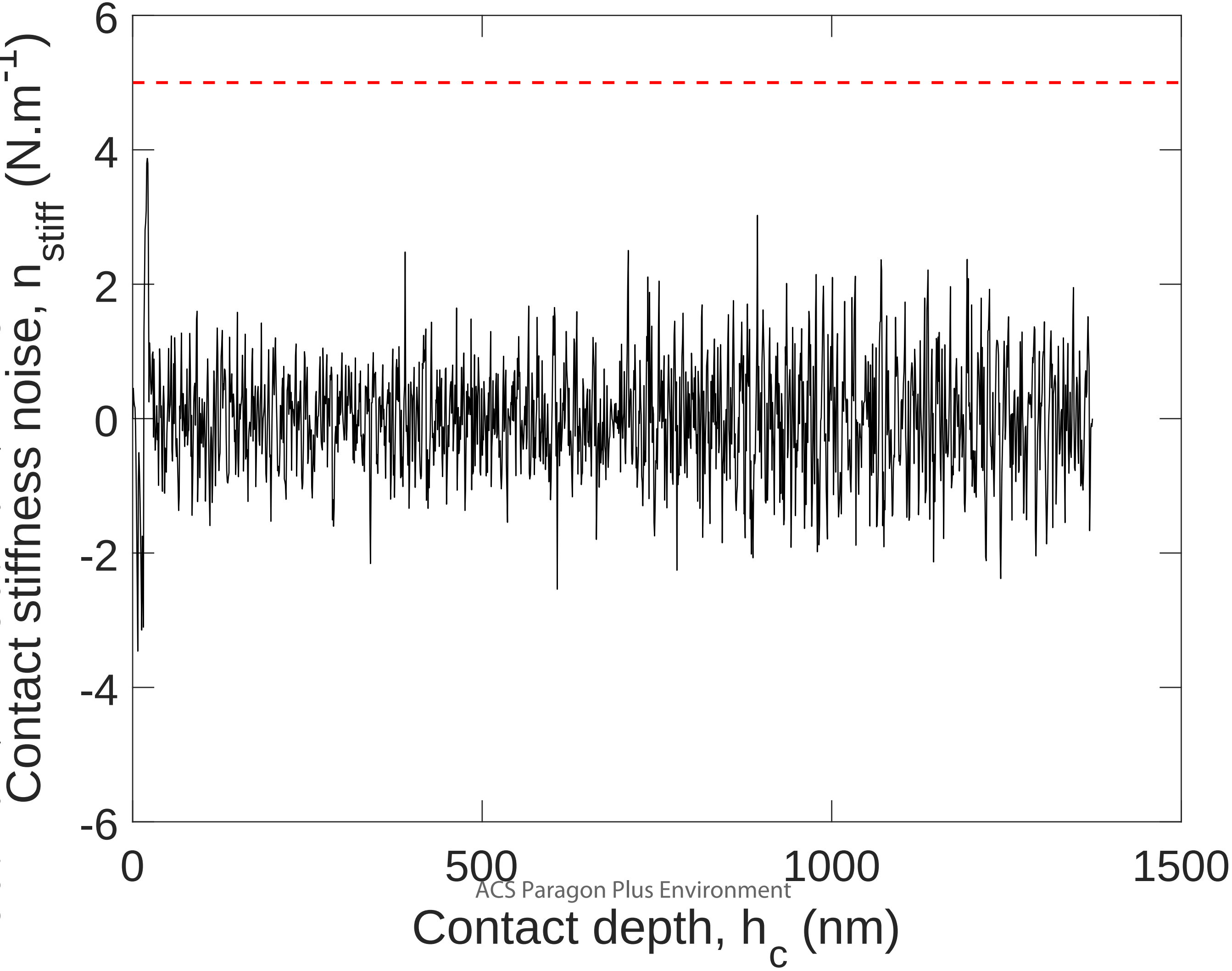
6
4
2
0
-2
-4
-6
0
500
1000
1500
Contact stiffness noise, n_{stiff} (N.m^{-1})
Contact depth, h_c (nm)

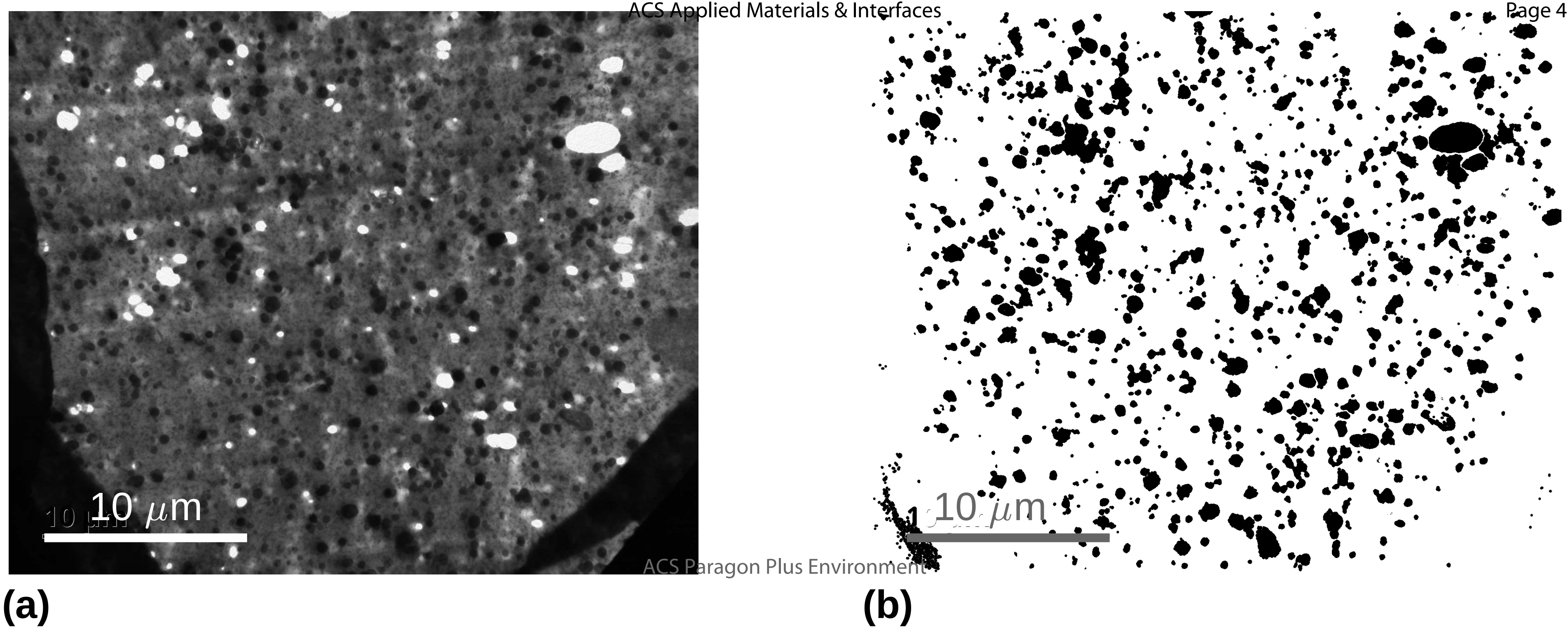
10 μm
(a)
10 μm
(b)

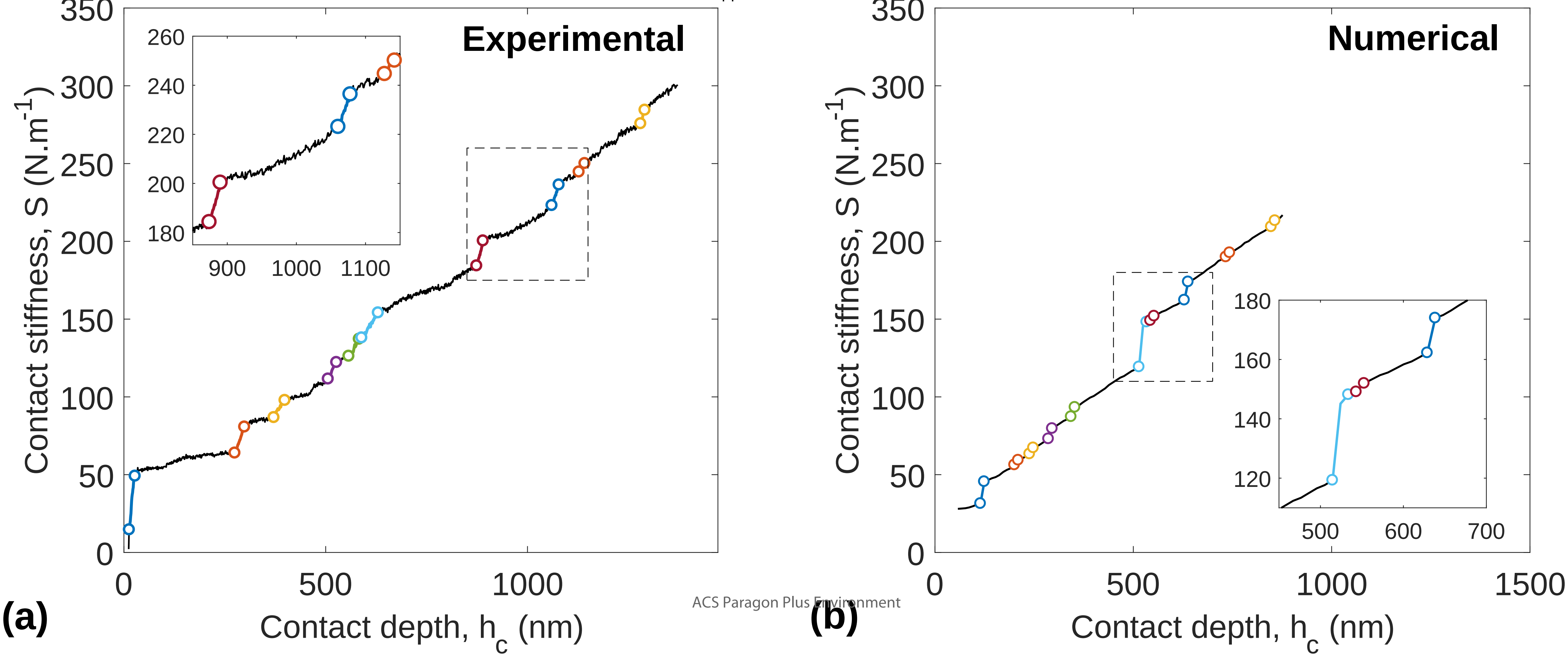
(a)
Experimental
Contact stiffness, S (N.m^{-1})
Contact depth, h_c (nm)
0
50
100
150
200
250
300
350
0
500
1000
180
200
220
240
260
900
1000
1100
(b)
Numerical
Contact stiffness, S (N.m^{-1})
Contact depth, h_c (nm)
0
50
100
150
200
250
300
350
0
500
1000
1500
120
140
160
180
500
600
700

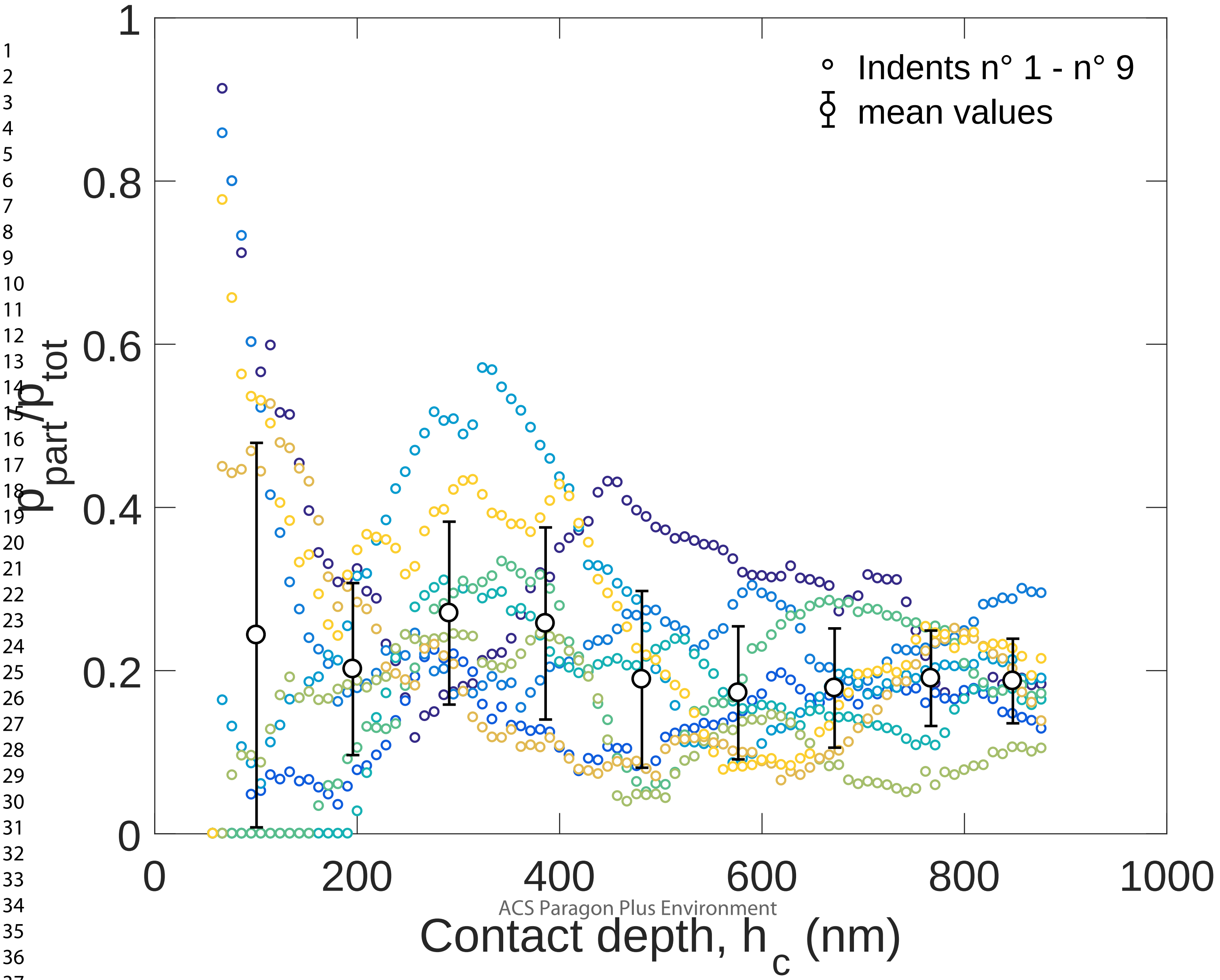
1
0.8
0.6
0.4
0.2
0
p_{part}/p_{tot}
0
200
400
600
800
1000
Contact depth, h_c (nm)
Indents n° 1 - n° 9
mean values

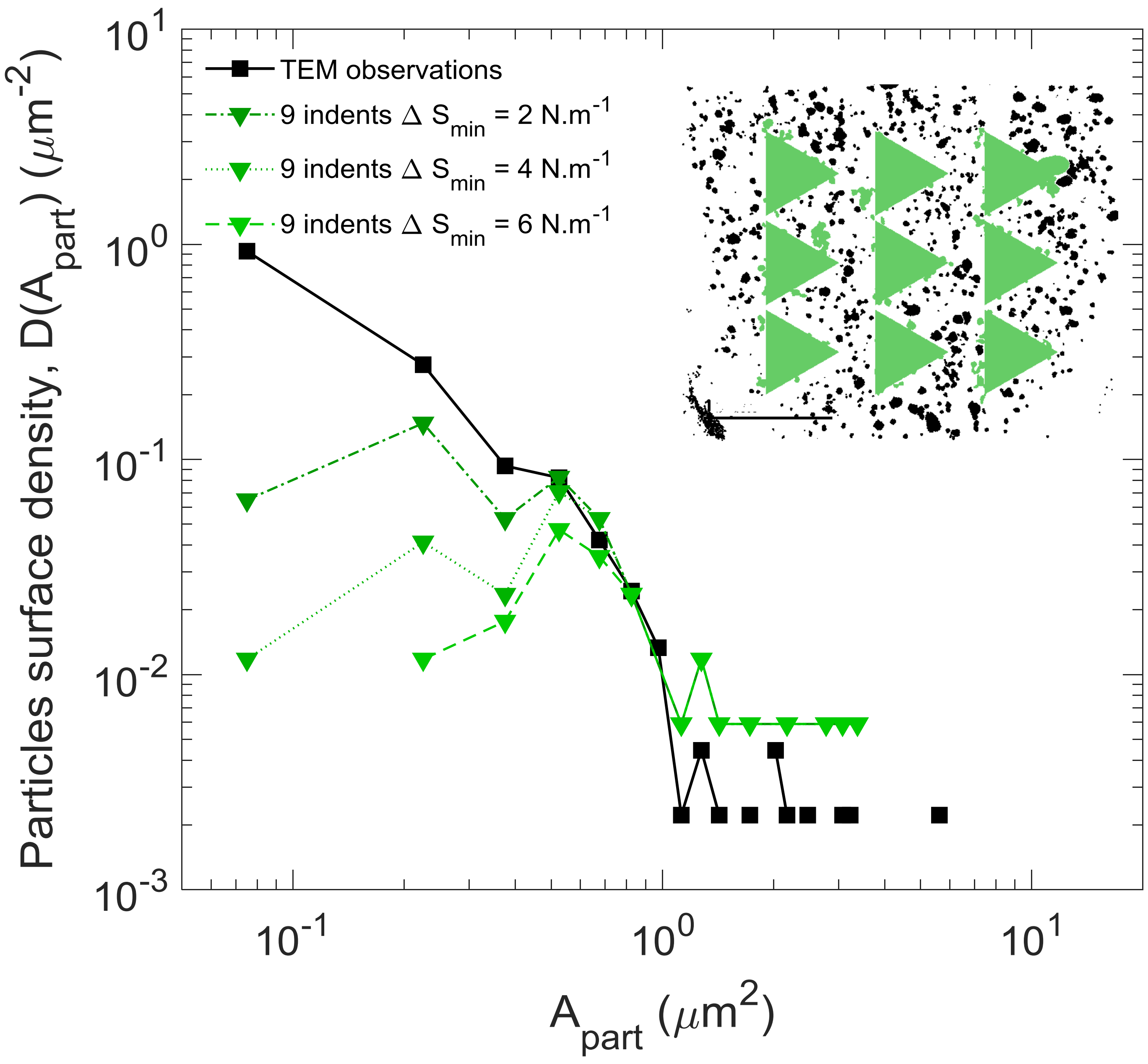
10^1
10^0
10^{-1}
10^{-2}
10^{-3}
Particles surface density, $D(A_{part})$ (μm^{-2})
TEM observations
9 indents ΔS_{min} = 2 N.m^{-1}
9 indents ΔS_{min} = 4 N.m^{-1}
9 indents ΔS_{min} = 6 N.m^{-1}
10^{-1}
10^0
10^1
A_{part} (μm^2)

(a)

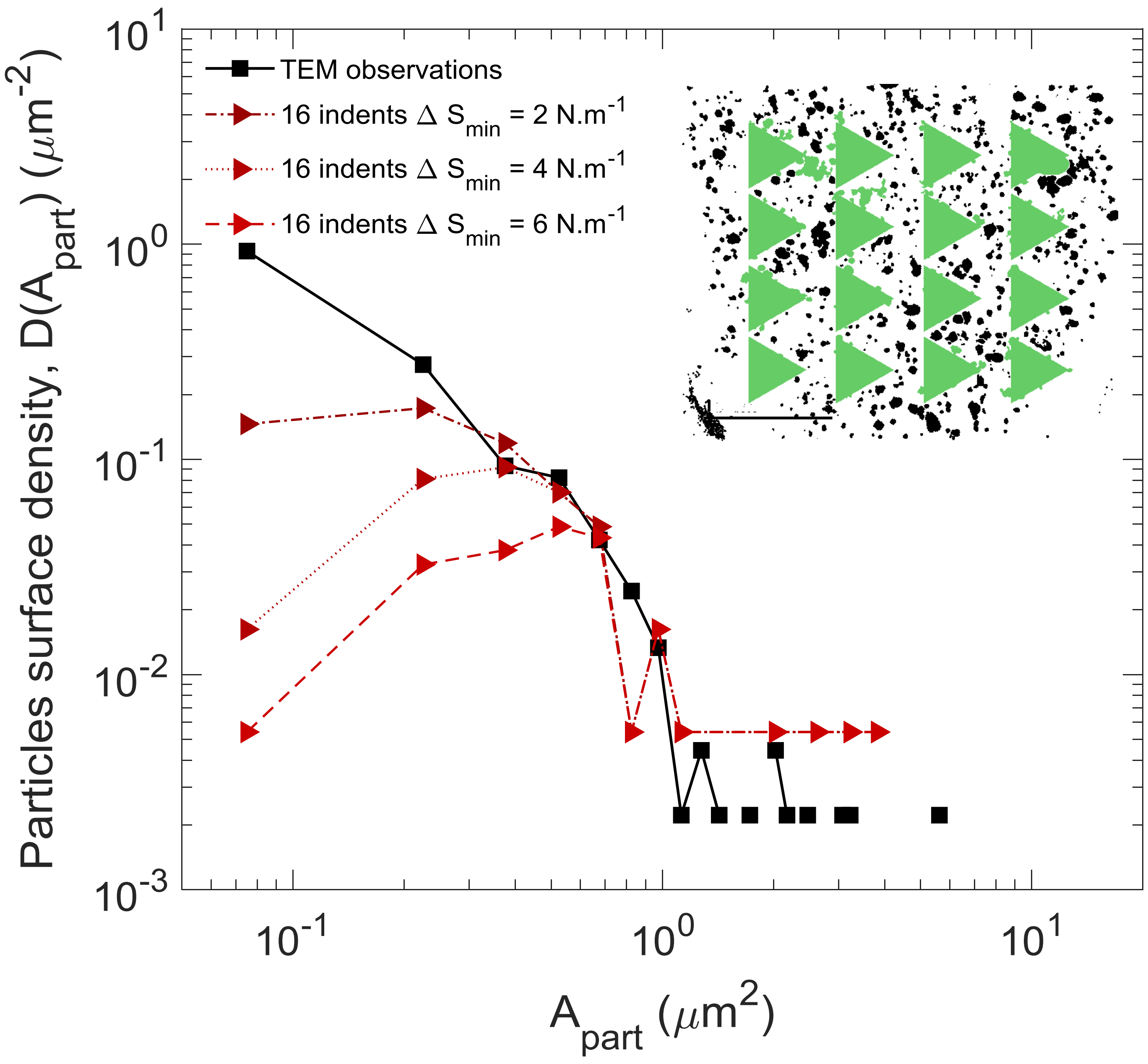
10^1
10^0
10^{-1}
10^{-2}
10^{-3}
Particles surface density, $D(A_{part})$ (μm^{-2})
TEM observations
16 indents ΔS_{min} = 2 N.m^{-1}
16 indents ΔS_{min} = 4 N.m^{-1}
16 indents ΔS_{min} = 6 N.m^{-1}
10^{-1}
10^0
10^1
A_{part} (μm^2)

(b)

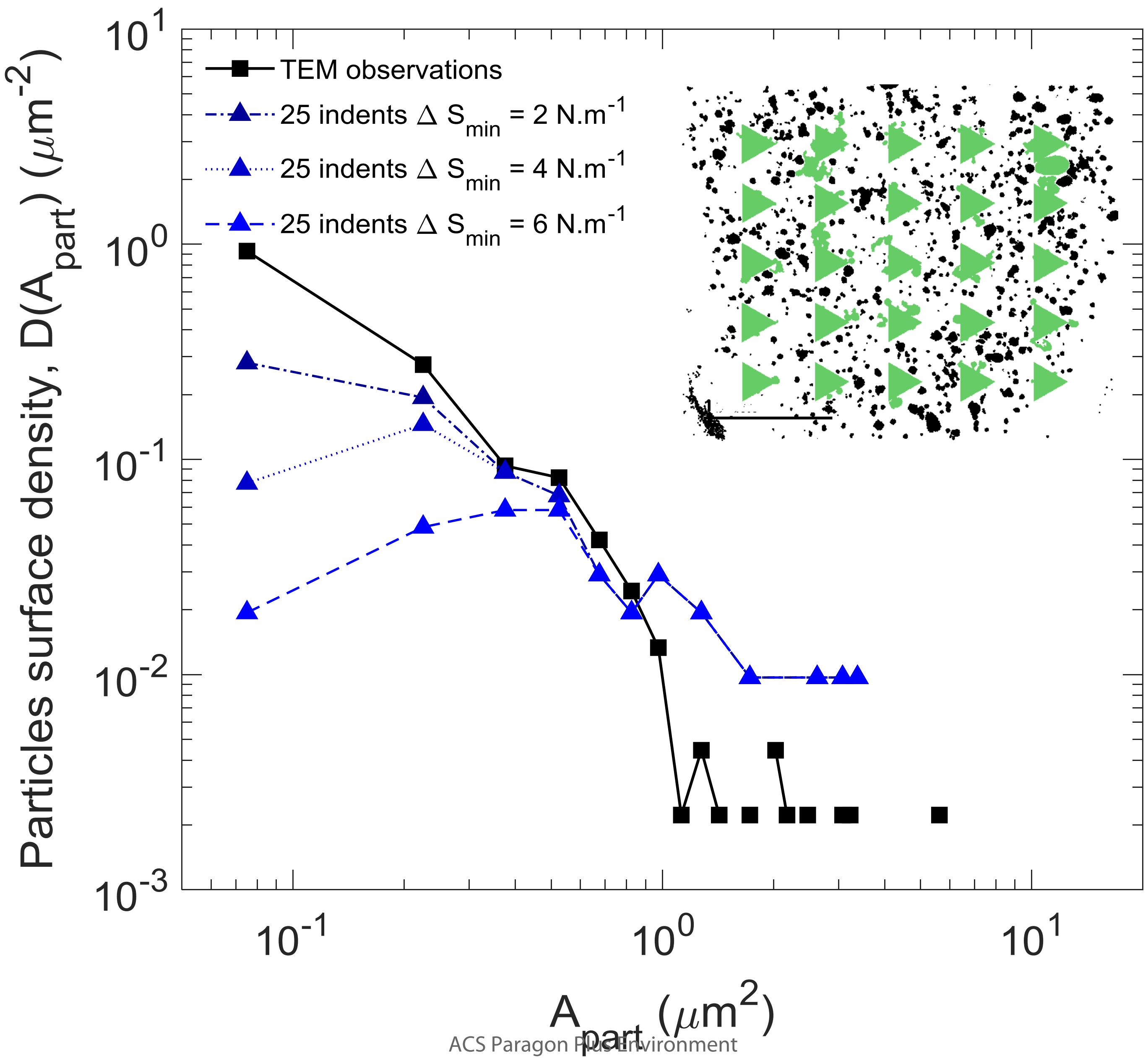
10^1
10^0
10^{-1}
10^{-2}
10^{-3}
Particles surface density, $D(A_{part})$ (μm^{-2})
TEM observations
25 indents ΔS_{min} = 2 N.m^{-1}
25 indents ΔS_{min} = 4 N.m^{-1}
25 indents ΔS_{min} = 6 N.m^{-1}
10^{-1}
10^0
10^1
A_{part} (μm^2)

(c)

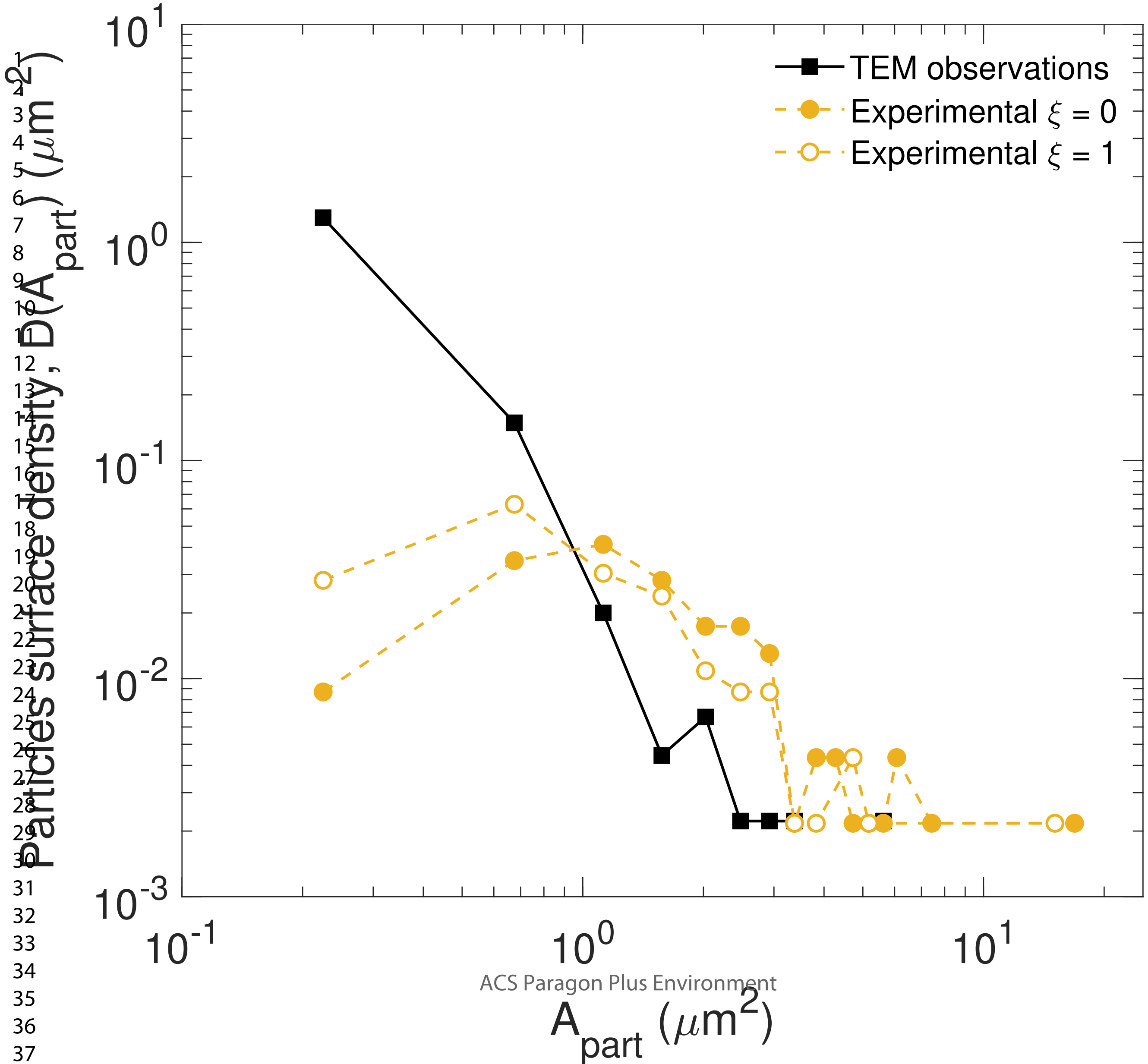
TEM observations
Experimental ξ = 0
Experimental ξ = 1
Particles surface density, $D(A_{part})$ (μm^2)
10^1
10^0
10^{-1}
10^{-2}
10^{-3}
10^{-1}
10^0
10^1
A_{part} (μm^2)

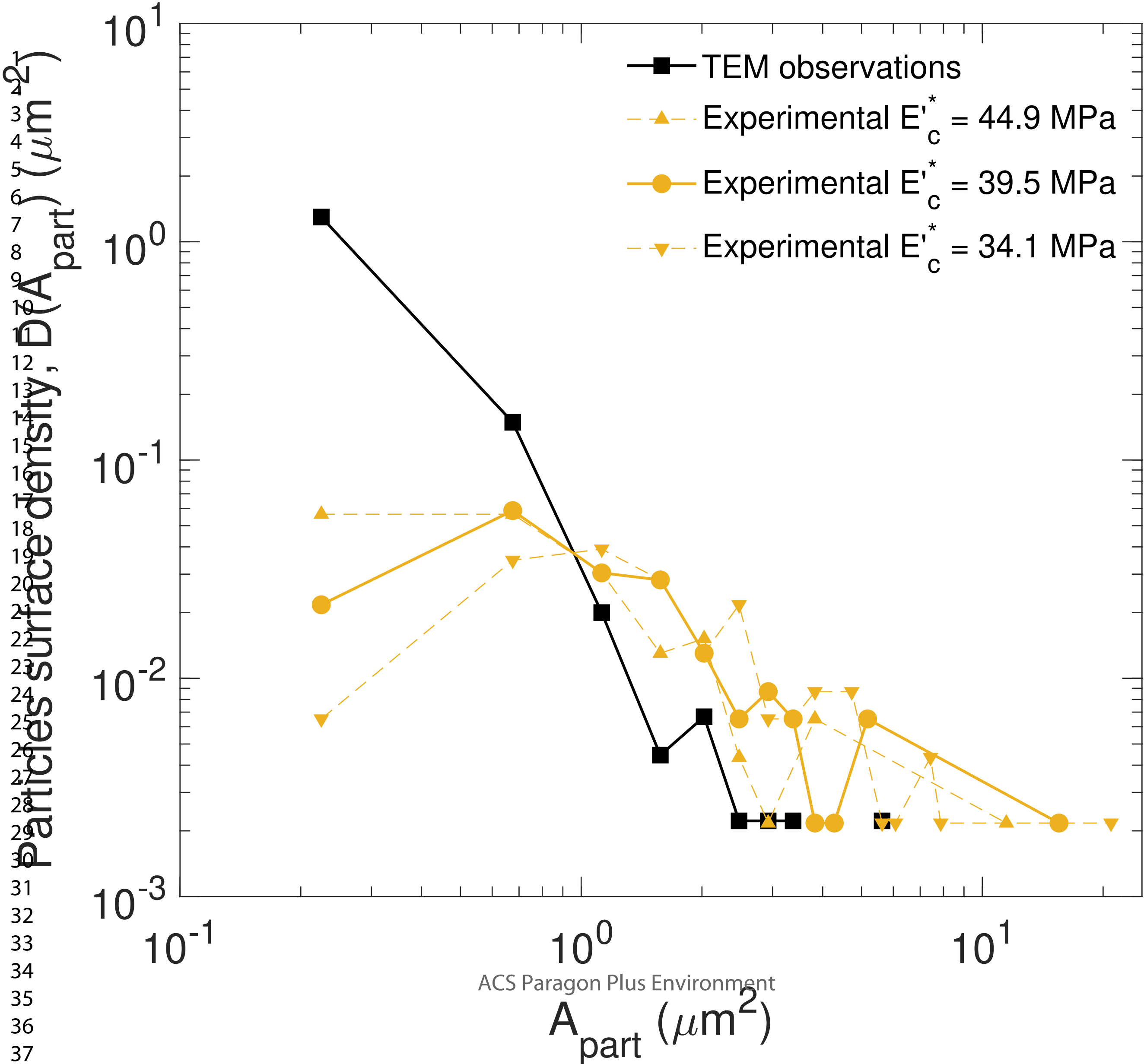
TEM observations
Experimental E'^{*}_{c} = 44.9 MPa
Experimental E'^{*}_{c} = 39.5 MPa
Experimental E'^{*}_{c} = 34.1 MPa
Particles surface density, $D(A_{part})$ (μm^{-2})
A_{part} (μm^2)
10^{1}
10^{0}
10^{-1}
10^{-2}
10^{-3}
10^{-1}
10^{0}
10^{1}

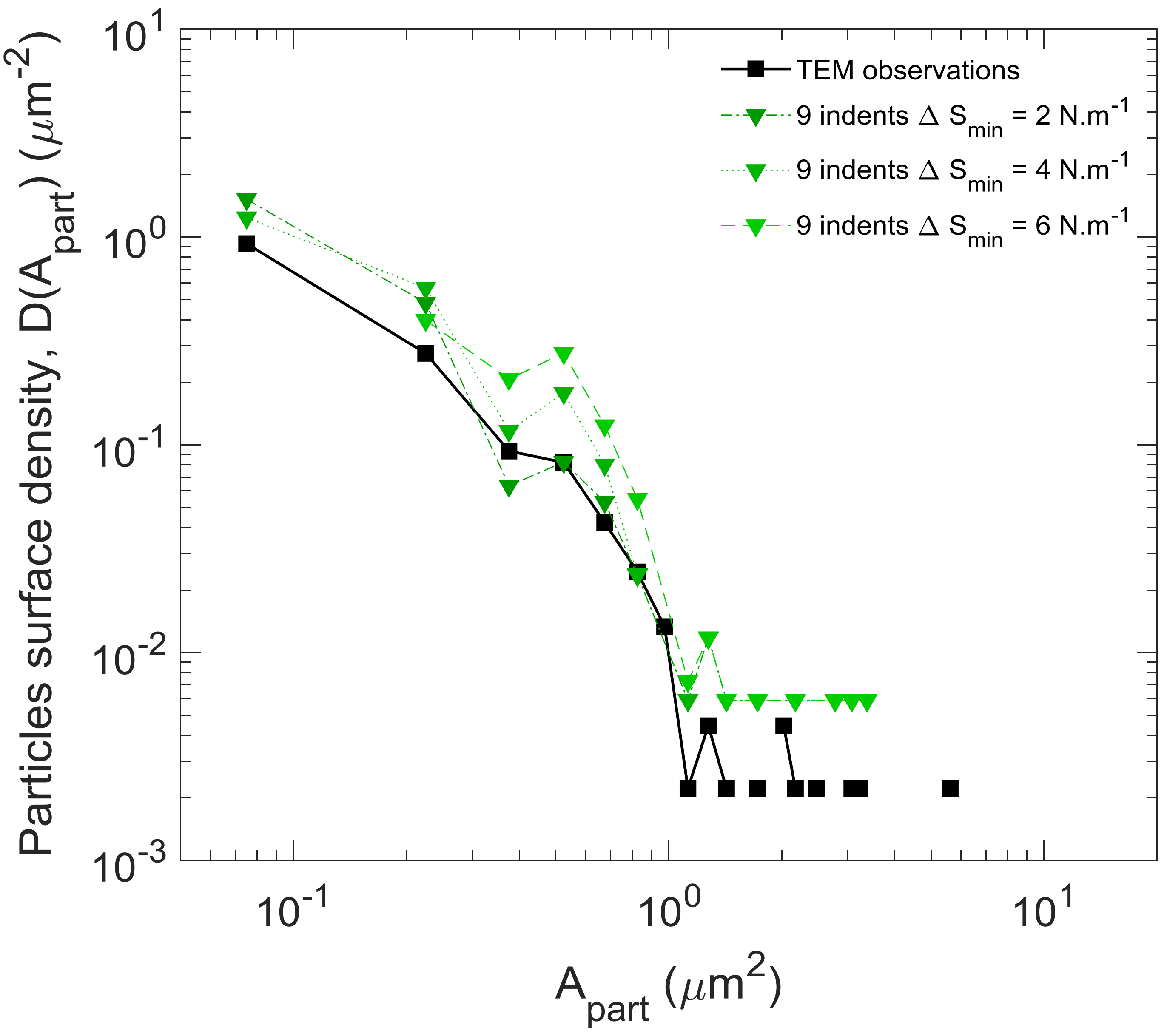
Particles surface density, D(A_part) (μm^-2)
A_part (μm^2)
10^1
10^0
10^-1
10^-2
10^-3
10^-1
10^0
10^1
TEM observations
9 indents Δ S_min = 2 N.m^-1
9 indents Δ S_min = 4 N.m^-1
9 indents Δ S_min = 6 N.m^-1

(a)

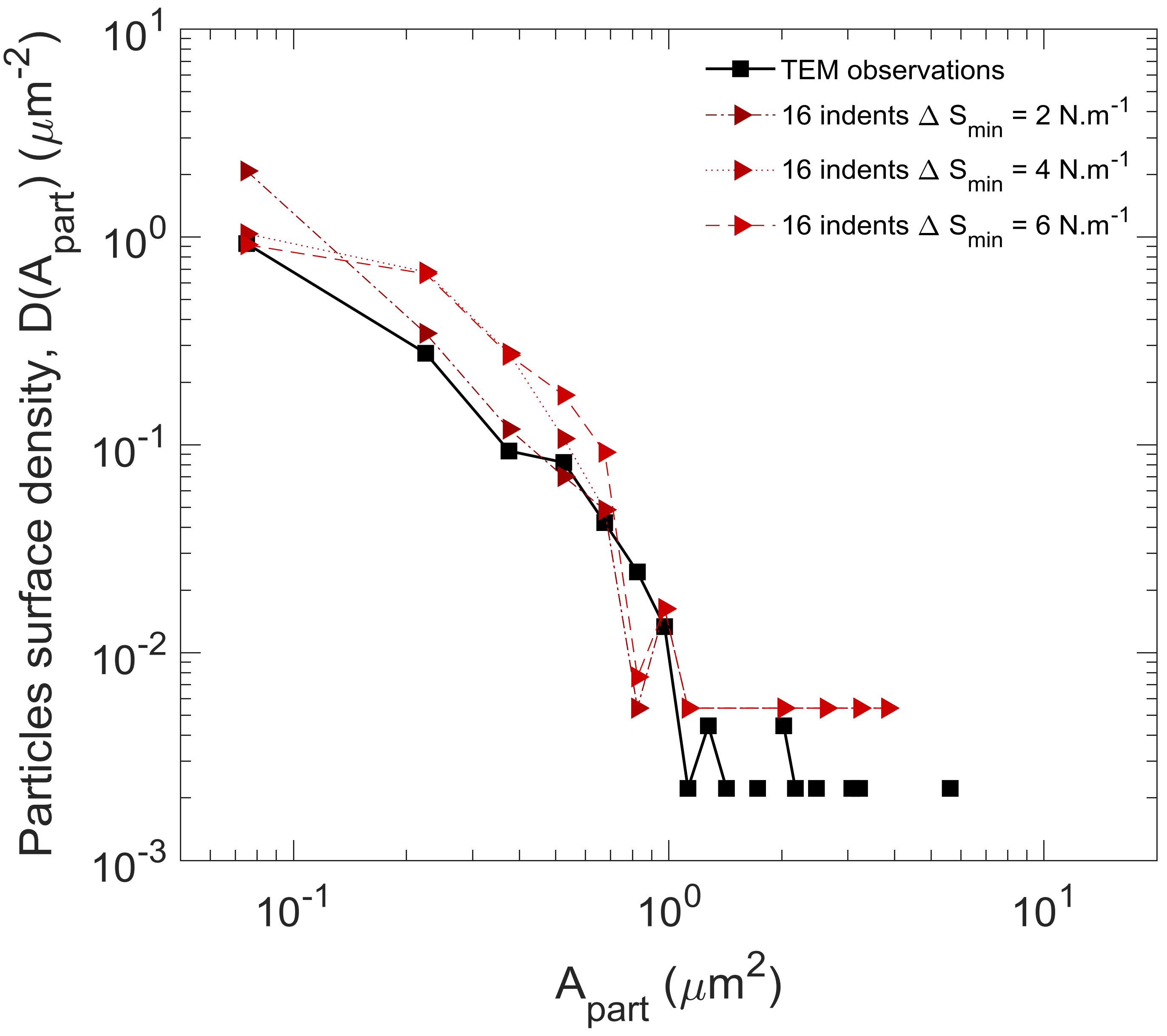
Particles surface density, D(A_part) (μm^-2)
A_part (μm^2)
10^1
10^0
10^-1
10^-2
10^-3
10^-1
10^0
10^1
TEM observations
16 indents Δ S_min = 2 N.m^-1
16 indents Δ S_min = 4 N.m^-1
16 indents Δ S_min = 6 N.m^-1

(b)

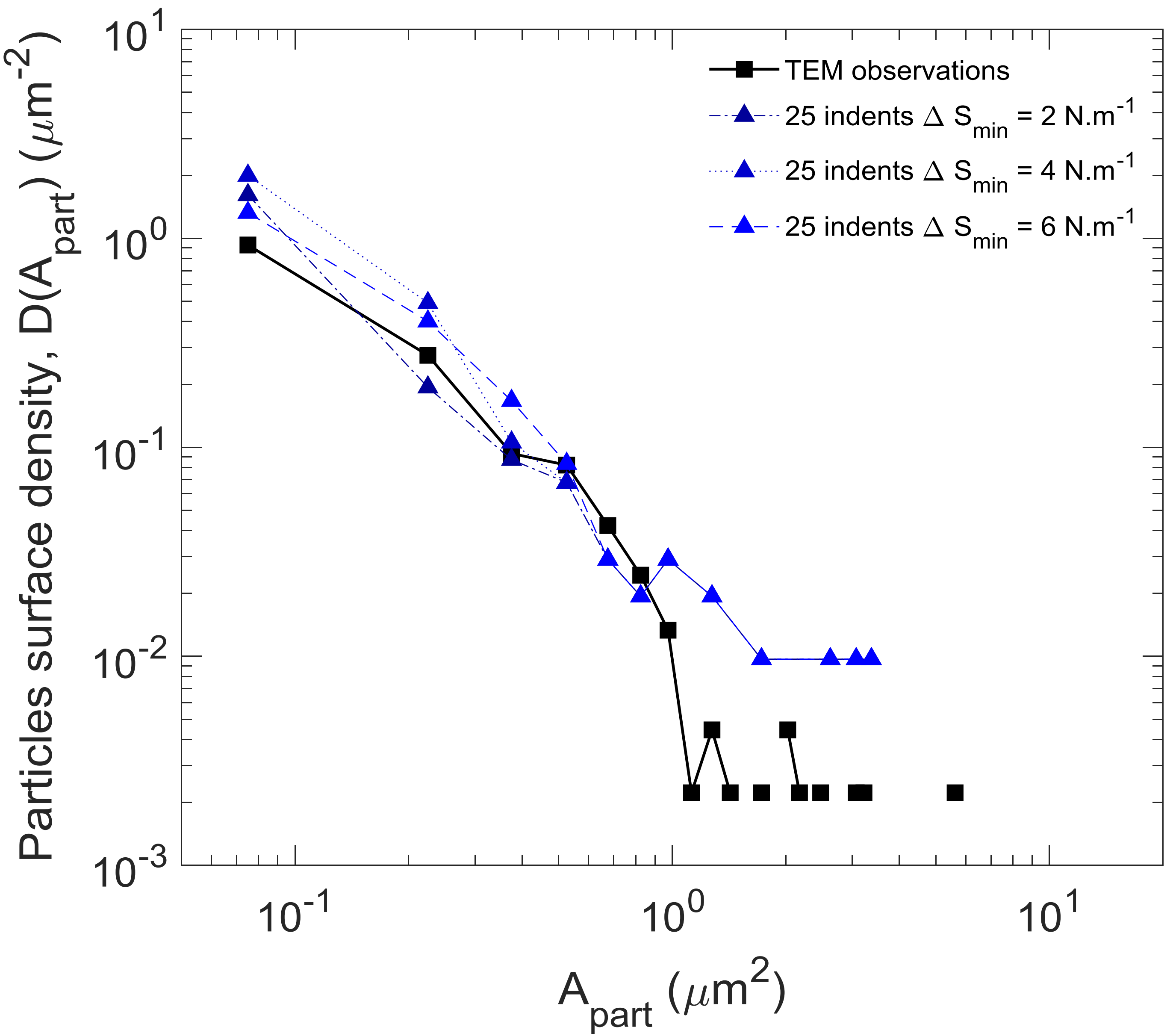
Particles surface density, D(A_part) (μm^-2)
A_part (μm^2)
10^1
10^0
10^-1
10^-2
10^-3
10^-1
10^0
10^1
TEM observations
25 indents Δ S_min = 2 N.m^-1
25 indents Δ S_min = 4 N.m^-1
25 indents Δ S_min = 6 N.m^-1

(c)

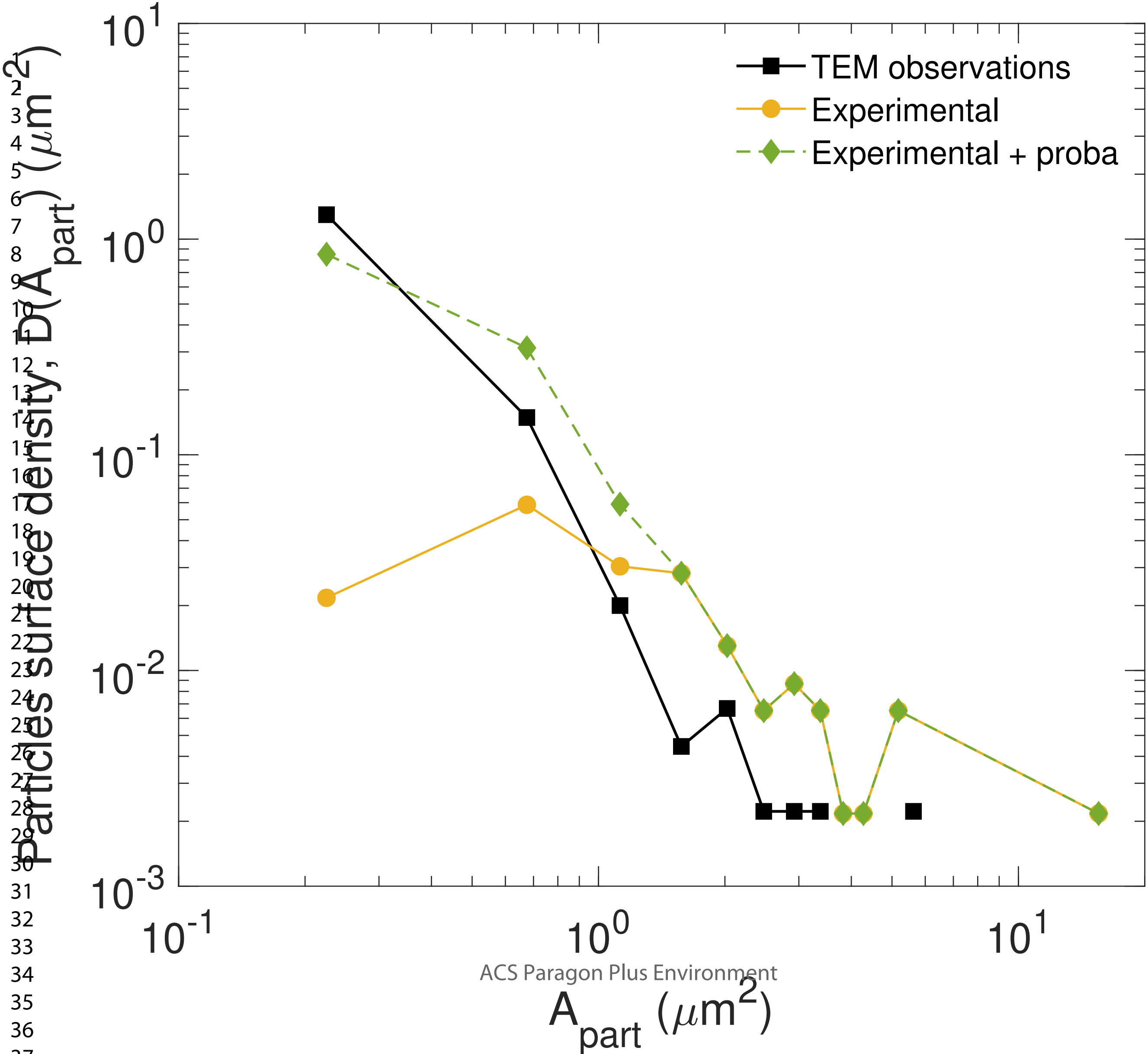
TEM observations
Experimental
Experimental + proba
Particles surface density, $D(A_{part})$ (μm^2)
10^1
10^0
10^{-1}
10^{-2}
10^{-3}
10^{-1}
10^0
10^1
A_{part} (μm^2)

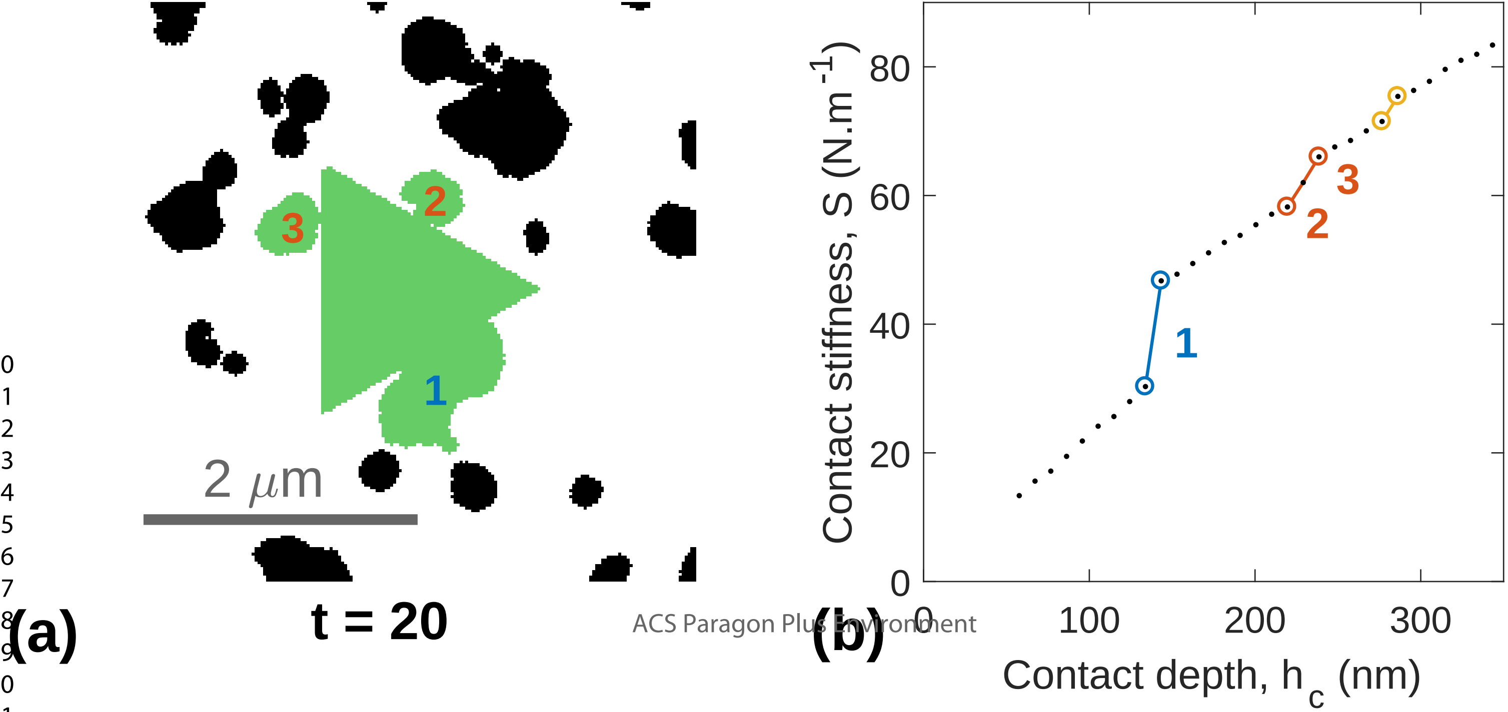
(a)
2
3
1
2 μm
t = 20
(b)
Contact stiffness, S (N.m^{-1})
Contact depth, h_c (nm)
0
20
40
60
80
0
100
200
300
1
2
3

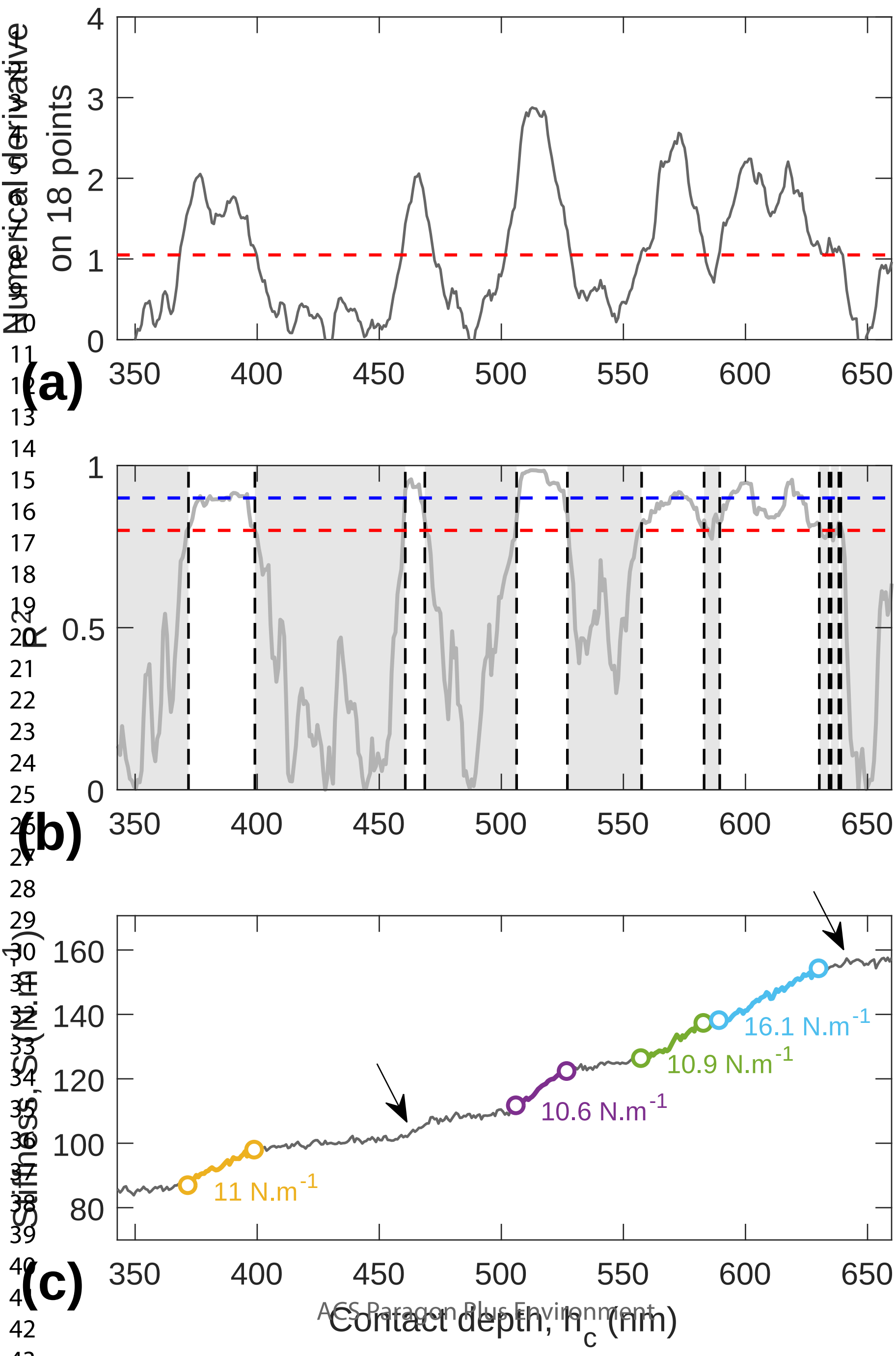
Numerical derivative
on 18 points
4
3
2
1
0
350
400
450
500
550
600
650
(a)
R^2
1
0.5
0
350
400
450
500
550
600
650
(b)
Stiffness, S (N.m-1)
160
140
120
100
80
11 N.m-1
10.6 N.m-1
10.9 N.m-1
16.1 N.m-1
350
400
450
500
550
600
650
(c)
Contact depth, hc (nm)

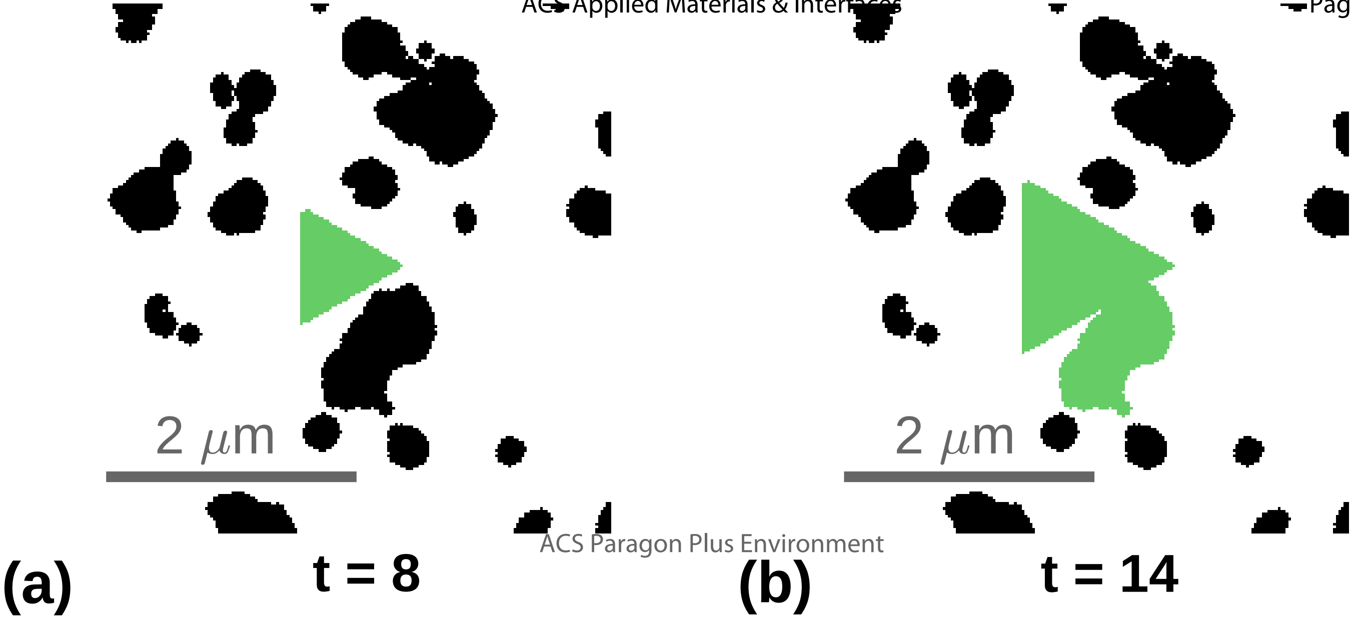
2 μm
(a)
t = 8
2 μm
(b)
t = 14